Department of Physics and Astronomy

University of Heidelberg

Bachelor Thesis in Physics

submitted by

Felix Schlepper

born in Wiesbaden (Germany)

2021

Differential analysis of the ALICE TRD anode currents

This Bachelor Thesis has been carried out by Felix Schlepper at the

Physikalisches Institut in Heidelberg

under the supervision of

Priv. Doz. Dr. Yvonne Pachmayer

Abstract

In order to accurately correct for space-charge distortions in the ALICE Time Projection Chamber in LHC Run 3, stable operation and a detailed understanding of the anode currents of the ALICE Transition Radiation Detector (TRD) at high luminosities is crucial. Therefore, tests at these expected high luminosities were performed in LHC Run 2. In this thesis, the expected linear correlation of the currents and the measured luminosity was parametrised. Additionally, a visible cross section was calculated from van der Meer scans using the anode currents of the TRD. Furthermore, the desired stable operation of the currents at high luminosity could be confirmed. Lastly, an algorithm for the early detection of chaotic currents of individual TRD chambers is presented. By detecting this type of chaotic current and subsequently reducing the applied voltage the lifetime of a chamber can be prolonged.

Kurzfassung

Damit man die Verzerrung der Driftspuren der Elektronen, welche durch Ansammlung der Raumladungen im Detektorvolumen der ALICE Zeitprojektionskammer verursacht wird, im LHC Run 3 korrigieren kann, braucht man ein gutes Verständnis und ein stabiles Verhalten der Anodenströme des ALICE Übergangsstrahlungsdetektors (TRD) bei hoher Luminosität. Daher wurden in Run 2 schon Tests bei den zu erwarteten Luminositäten durchgeführt. Im ersten Teil dieser Arbeit wird die lineare Korrelation von Anodenströmen und Luminosität parametrisiert. Hier bestätigte sich diese lineare Korrelation und auch das benötigte stabile Verhalten der Ströme bei hohen Luminositäten. Zusätzlich wurde ein sichtbarer Wirkungsquerschnitt mit Hilfe der Anodenströmen aus den Daten eines van der Meer scans berechnet. Im Anschluss wurde ein Algorithmus zur Detektion chaotischer Ströme von defekten Kammern des TRDs entwickelt. Durch das Identifizieren dieser defekten Kammern und der Reduktion der anliegenden Spannung, kann die Lebenszeit dieser Kammern verlängert werden.

Table of Contents

1 Introduction

1.1 Motivation

Shortly after the Big Bang, the universe was in a state of hot and dense matter, called **q**uark-**g**luon **p**lasma (**QGP**). After expansion and cooling of the universe, hadronic matter as it also surrounds us today emerged from the QGP. In this short lived state, quarks and gluons are quasi deconfined and interactions are dominated by the strong force. Probing this state of matter allows gaining further insight into the theory of the strong interaction.

The theory of quark-gluon plasma is neatly explained within the Standard Model and is tied up together in the field theory of quantum chromodynamics (QCD). Here, quarks are elementary particles carrying an electric charge and colour. Interaction is mediated by colourful gluons. The fact that gluons have colour themselves is crucial. This leads to self-coupling and therefore to a more complex theory with different properties to quantum electrodynamics (QED). One of these properties, is that the potential for the strong interaction increases linearly with distance of the partaking quarks. Hence, quarks can only separate themself if enough energy is available to form new quark-antiquark pairs. This leads to the fact that colourful states cannot be observed (colour confinement), thus quarks cannot occur freely in nature. However, in the QGP the temperature and energy density is high enough, that individual quarks themselves 'forget their partner' and free colour charges are allowed to exist. Intense experimental effort is required to produce such high energies in order to study quark matter.

A few minor remarks on the Standard Model (Figure 1.1) are given here, since it has been and continues to be a milestone of modern physics. Probed consistently over decades, it accurately predicts the properties of many fundamental particles and interactions. With the discovery of the Higgs boson in year 2012 as the latest big confirmation. Despite it being a huge success, the Standard Model falls short of incorporating all fundamental interactions (gravity being left out) and it leaves some physical phenomena unexplained, such as dark matter [1].

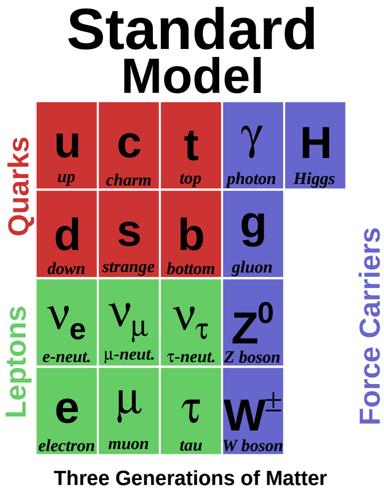

Figure 1.1: Fundamental particles of the Standard Model (SM) with three generations of fermions, the gauge bosons and the Higgs boson. For every fundamental fermion an anti-particle with opposite charge exists.

Which is why probing the Standard Model and therefore the QGP is so important. Clearly knowing where theory and experiment deviate can lead to formulating new and better models.

To explore the properties of the strongly interacting matter (QGP), **A** **L**arge **I**on **C**ollider **E**xperiment (**ALICE**) was built. Located at the **L**arge **H**adron **C**ollider (**LHC**) at the European Organization for Nuclear Research (CERN), ALICE investigates collisions of heavy nuclei (Pb+Pb collisions), in which the QGP is produced. Convenient probes for the study of the QGP are e.g. heavy flavour hadrons and the J/ψ mesons [2]. Due to their short lifetime, J/ψ mesons [3] are only really detectable via their decay products. Lepton pair production, while not the most dominant decay mode, still is a major contributor with $(5.971 \pm 0.032)\%$ of the total branching ratio. Furthermore, the fact that leptons do not participate in the strong interaction, makes them more interesting and very accessible. One of the detectors, that examines the final state particles of these collisions in ALICE, is the **T**ransition **R**adiation **D**etector (**TRD**), for more information on the TRD see Chapter 2.

1.2 Goal

This thesis focuses on the anode currents of the ALICE TRD chambers at high luminosity in view of Run 3. In order to correct more accurately for space-charge distortions in the ALICE Time Projection Chamber, as pointed out by [4], thorough knowledge of the these currents is crucial.

The goals of this thesis in detail are to parametrize the correlation between anode currents and luminosity, and determine whether or not the anode currents are stable at the luminosities expected in LHC Run 3 and 4. Moreover, how to recognise chaotic currents in the TRD chambers (Section 4.3) in order to reduce the operational voltage and prolonging the chamber's lifetime. Furthermore, determine if one can infer a cross section and luminosity from van der Meer scans with the TRD anode currents alone (Section 4.4).

1.3 Outline of this thesis

The following Chapter 2 introduces the ALICE TRD, its gas system, which will become significant later and important concepts. Chapter 3 presents the analysis strategy for the different analyses performed, properly documents the workflow and provides various links to the source files used. The results of these analyses are provided and discussed in Chapter 4. The summary and outlook are given in Chapter 5.

2 | ALICE

The following chapter gives a brief introduction into the physics of the ALICE Transition Radiation Detector (TRD) [5], followed by a short description of the read-out chambers, the gas system and in the end performance measures relevant for this thesis are introduced.

2.1 Transition Radiation Detector

As described in Section 1.1, electrons are of particular interest in the study of the QGP. For this reason, good electron identification is essential. The TRD provides excellent electron pion separation up to momenta of 100 GeV.

Transition Radiation (TR) can occur if a fast charged particle ($\beta\gamma \geq 1000$ [6]) crosses the boundary of two media with different dielectric constants. This is due to the realignment of the electromagnetic fields of the crossing particle in the second medium, ensuring homogeneity of Maxwell's equations, see [7]. Therefore, TR is the energy difference of the two inhomogeneous solutions of Maxwell's equations in each medium separately, which is typically in the hard x-ray regime. Pions only start producing TR at a momentum of about 140 GeV and electrons much earlier (0.5 GeV).

For this reason, TR can be exploited to efficiently differentiate electrons and pions at momenta relevant for ALICE. The photon yield of TR is at the order of the fine structure constant ($\alpha \approx 1/137$), consequently many boundary crossings are needed in detectors to reliably produce a signal.

In practice, TR photons are produced in a radiator, which in ALICE TRD consists of polypropylene fibre mats giving many boundaries. A chamber of the ALICE TRD consist of a radiator mounted in front of a drift chamber filled with a xenon-based gas mixture with a multi-wire proportional chamber (MWPC) within the same gas volume, making up the amplification

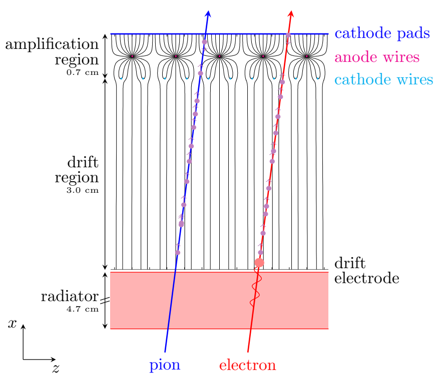

(a) Schematic sideways cross section of a TRD chamber [5].

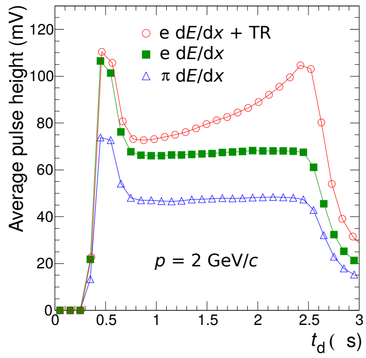

(b) Average pulse height as a function of drift time for pions and electrons with and without radiator [5].

Figure 2.1: Schematic TRD chamber and measured pulse height spectrum

region at the end. All this is schematically drawn in Figure 2.1a.

The measured pulse height can be seen in Figure 2.1b. The fast charged electrons ($\beta\gamma \geq 1000$) enter the radiator, possibly produce TR and subsequently enter the drift chamber. The first peak for both particles (electron and pion) comes from the primary charged particle. The following plateau is due to the ionization trail produced by the primary particle interacting with a gas in the drift chamber. For electrons with TR a second peak can be seen. This is due to the produced TR photon depositing its energy in the gas close after the radiator in the drift chamber. TR photons interact via the photoelectric effect. The pion does not produce a TR photon with the same momentum as it is much heavier.

Photons should preferably be absorbed near the entrance of the drift chamber, as to have maximal signal separation between TR and the primary particle. To fulfil this near entrance absorption requirement, a gas mixture consisting of 85% Xe for fast absorption and 15% CO_2 as a quencher is chosen. The purpose of the CO_2 is to limit multiple pulsing by secondary electrons and it additionally makes the detector fireproof.

A full picture of ALICE can be found in Figure 2.2. Around the interaction point the inner tracking system (ITS) is built. On one side of the ITS the muon absorber is placed to suppress all particles except muons. It is made of carbon and concrete [8]. The ITS is surrounded by the time projection chamber (TPC) and then the TRD. Other, for this thesis unimportant, detectors follow. The whole system is surrounded by a big solenoid magnet with a metal door on one side of the detector and the muon arm on the other.

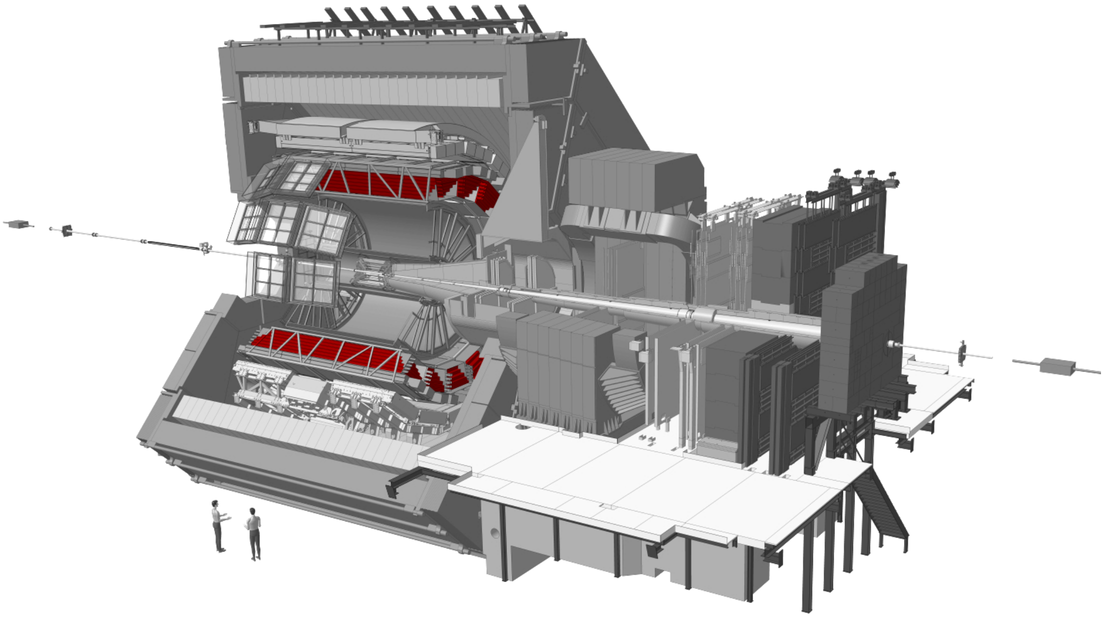

Figure 2.2: Full schematic picture of the ALICE Detector is shown. The TRD is highlighted in red [9].

2.2 Read-out pads

The TRD, shown in Figure 2.2, is located after the TPC at a radial distance from 2.90 m to 3.68 m from the beam axis [5]. The ϕ-direction coverage is split into 18 sectors called supermodules as can be seen in Figure 2.3. Along the beam direction (z_{lab}), the coverage is split into five stacks. These stacks are numbered from 0 to 4, where stack 0 is at A-side (close to the magnet door) and stack 4 at the C-side (close to the muon arm). Additionally, each stack hosts 6 layers (numbered 0 to 5), where layer 0 is closest to the collision point and layer 5 farthest away. Each supermodule thus hosts 30 chambers, allowing the ALICE TRD to host a total of 540 chambers (18 sectors $\times$ 6 layers $\times$ 5 stacks). In order to minimise material in front of the PHOS detector, the middle stacks in sectors 13-15 are not installed. Thus 522 exist in total, although not all are in nominal working condition, as will be discussed in Section 3.2. A chamber is uniquely identified by its label. The label folllows an easy naming convention, given by "sector_stack_layer". For example chamber 06_0_1 is located in the sixth sector, 0th stack and 1st layer.

One must pay special attention to the size of the TRD chambers, since their size increases radially and changes along the beam direction, see Figure 2.4. This must also be corrected for later on, as the chamber size is directly proportional to the anode current produced. The chamber size for each sector can be found in Table 2.1. The increase in chamber size in radial direction is to minimize the differences in full solid angle coverage in a stack. The calculated full

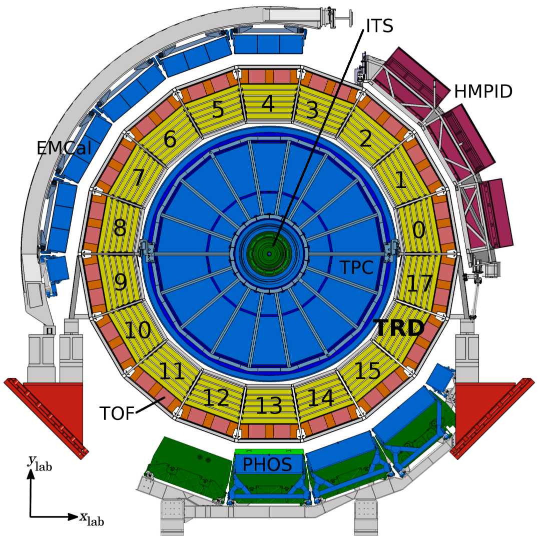

Figure 2.3: Schematic cross section of the ALICE detector. The central barrel detectors cover the pseudorapidity range $|\eta| \lesssim 0.9$ and are located inside the solenoid magnet, which provides a magnetic field with strength $B = 0.5$ T along the beam direction. The TRD supermodules are highlighted in yellow [5].

solid angle coverage of a chamber can be found in Table 2.2.

Stack	Layer 0	Layer 1	Layer 2	Layer 3	Layer 4	Layer 5
2	1060x1060	1060x1060	1060x1060	1060x1060	1060x1060	1060x1060
0,1,3,4	1200x1200	1200x1200	1270x1270	1340x1340	1410x1410	1430x1430

Table 2.1: Read-out chamber size (mm^2) [10].

stack	Layer 0	Layer 1	Layer 2	Layer 3	Layer 4	Layer 5
0	0.0786	0.0757	0.0780	0.0801	0.0820	0.0806
1	0.1279	0.1196	0.1241	0.1283	0.1322	0.1279
2	0.1209	0.1116	0.1034	0.0960	0.0894	0.0834
3	0.1279	0.1196	0.1241	0.1283	0.1322	0.1279
4	0.0786	0.0757	0.0780	0.0801	0.0820	0.0806

Table 2.2: Solid angle covered by a chamber (steradian), calculated with [11].

The MWPCs are the most important part of the detector for this thesis, since the currents produced by them will be analysed. The MWPCs consist of an array of wires at high voltage (anode) running equally spaced (7.25 mm [5]) between two cathode plates, see Figure 2.5. Ions and electrons are accelerated along the strong electromagnetic field close to the anode wire,

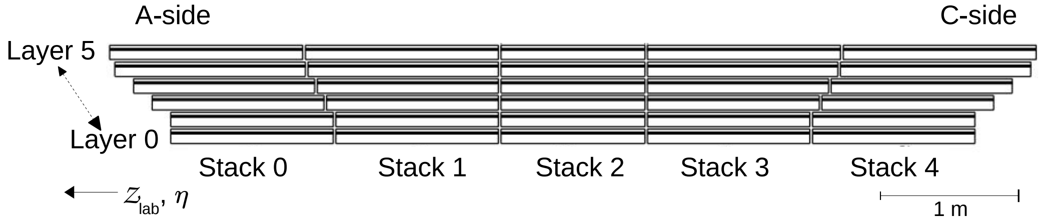

Figure 2.4: Cross section (longitudinal view) of a supermodule [5].

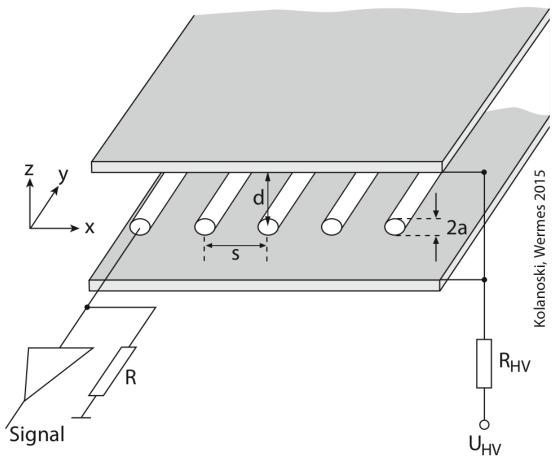

Figure 2.5: Schematic Drawing of a MWPC. The signal drawn here is synonymous to the often mentioned anode current [12].

causing the formation of ionization avalanches. This avalanche is collected by the nearest anode wire, inducing a measurable signal, which, as the name suggest, is proportional to the energy lost.

During data taking, the MWPCs are operated at a nominal anode voltage of about 1530 V. However, each chamber is individually supplied with a specific voltage, as to correct for differences in gain. The spread of these voltages is around 90 V (6% of $V_{nominal}$) for the working chambers. This is checked periodically, once or twice a year, to make sure all chambers have the same gain. During startup, the channels are ramped up to 1000 V at steps of 6 V/sec. At 1000 V they are held to achieve equilibrium and afterwards further ramped up to their final voltage with another break at 1250 V. The reason for this three stage startup is that the LHC beam initially is not stable or fully injected. If a particle from the beam would hit detector material, the luminosity would drastically spike beyond the design limits of the detector. However, at 1000 V the gain is negligible and not much current would be produced. This makes the startup phase for the detector much safer.

2.3 Gas System

Controlling the gas quality is crucial for the detector operation since both gain values and drift velocity need to be accurately known and uniform for particle identification and online tracking [5]. The importance of monitoring the gas system has already been thoroughly investigated and stressed in [13]. Here, one can already deduce that the gas composition has to be well known to account for any irregularities concerning the analysed anode currents. Especially, the influence of gases like O_2, H_2O and N_2 will be touched upon in Section 4.2. This thesis focuses on the most important parts of the gas system. A complete breakdown of the gas system can be found in [5].

Two cartridges with a volume of three litres including a copper catalyser comprise the purifier module. This module removes oxygen by oxidising copper chemically and removing water mechanically by absorption. Two semipermeable membrane cartridges, which consist of bundles of capillary polyimide tubes through which the gas mixture flows, separate CO_2 from Xe. As to safeguard each supermodule, a bubbler is installed, which ensures that the detector pressure always remains within ± 1.3 mbar relative to atmospheric pressure [5]. To avoid that other gases enter the bubblers, the external sides are connected to a continuous flow of N_2. Inevitably though, N_2 can build up through the backup system and leaks, contaminating the gas mixture.

The contamination by oxygen and water can be prevented by the above mentioned purifier. However, the N_2 contamination is much harder to control, making the admixture of N_2 continuos until special separation procedures are performed. This can be achieved by utilising the different freezing points of Xe and N_2. Due to the complexity and longevity of this process, it is done only during a long shutdown every one or two years, while the N_2 contamination continuos to increase.

2.4 Sub-detectors

In the following only sub-detectors of the ALICE detector relevant for this thesis will be discussed.

2.4.1 EMCal

The electromagnetic calorimeter (EMCAL) is a large sampling lead-scintillator of shashlik design with a cylindrical geometry. Located adjacent to the ALICE magnet coil at a radius of approximately 4.5 meters, covering the $-0.7 < \eta < 0.7$ acceptance [14]. Electromagnetic calorimeters measure the deposited energy of a particle from the electromagnetic showers in the active media. A sampling calorimeter comprises of alternating layers of absorber material to degrade the particle energy and active media to provide the detectable signal. Visible energy deposited in the active media of the calorimeter produces a detectable signal, proportional to the total energy deposited by the particle. This signal is then measured using photodiodes. The ALICE experts derive a instantaneous luminosity from the energy deposition in the EMCal for the high luminosity runs. This luminosity information is used in the analysis.

2.4.2 V0 detector

The V0 detector consists of two arrays of fast scintillator counters, covering the acceptance region $2.8 < \eta < 5.1$ and $-3.7 < \eta < -1.7$ [15] respectively. Both are installed on either side of the interaction point. The detector provides several functions, like a minimum bias trigger to differentiate real collision events from interactions of e.g. protons with residual gas in the vacuum chamber. For the purpose of this thesis, the V0 detector provides a measurement of the total trigger rate (interaction rate plus background rate) in proton-proton collisions as measured in van der Meer scans, see Section 2.5.2.

2.5 Important concepts

In the following concepts relevant for this thesis will be introduced.

2.5.1 Luminosity

Luminosity gives a measure of how many collisions are happening in a particle accelerator at a given time period. It is essentially the proportionality factor between the number of events per second dN/dt and the cross section σ:

$$\frac{dN}{dt} = \mathcal{L} \cdot \sigma$$

The unit for luminosities is therefore cm^{-2} s^{-1}. In [16] the luminosity for head-on collision for Gaussian beam profiles is defined as:

$$\mathcal{L} = \frac{N_1 N_2 f N_b}{4\pi\sigma_x\sigma_y}$$

where N_1 and N$_2$ denote the number of particles per bunch, f a revolution frequency, N_b the number of bunches and σ_x and σ_y the width of the beam profile. Some figures of merit for the LHC during Run 2 can be found in Table 2.3.

No. of bunches per proton beam N_b	2808
Number of turns per second f	11245
No. of protons per bunch (at start) $N_{1,2}$	$1.2 \cdot 10^{11}$

Table 2.3: Figures of merit for the LHC in Run 2 [17].

2.5.2 Van der Meer scans

Luminosity determination in ALICE at the LHC is largely based on the visible cross sections measured in **v**an **d**er **M**eer (**vdM**) scans. In Section 4.4, a luminosity will be derived from the TRD anode currents, in analogy to [15]. This is especially interesting, since the TRD is completely independent from the usually used V0 detectors.

In vdM scans the two beams (one rotating clockwise, the other rotating counter-clockwise around the LHC) are moved twice across each other in transverse directions x and y. Meaning, while one beam is fixed in position for head-on collisions, the other is being actively moved in x and y directions across the fixed one. This is being achieved by changing the electromagnetic field near the collision point to collimate both beams onto each other. As stated in [15], measuring the rate R of a reference process as a function of the beam separation Δx and Δy allows one the calculate the luminosity for head-on collisions of a pair of beams with particle intensities N_1 and N_2 as

$$L = \frac{N_1 N_2 f_{rev}}{(h_x h_y)}$$

where h_x, h_y are the effective beam widths in the two transverse directions and f_{rev} is the accelerator revolution frequency. The visible cross section $\sigma_{visible}$ for the chosen reference process is then

$$\sigma_{visible} = \frac{R\,(0,0)}{L}$$

In this thesis, the process rate R are the anode currents of the ALICE TRD. The effective beam widths are measured as the area below the $R\,(\Delta x, 0)$ and $R\,(0, \Delta y)$ curve (scan area), respectively, each divided by the head-on rate $R\,(0,0)$, yielding

$$h_x = \frac{\int d\Delta x R\,(\Delta x, 0))}{R\,(0,0)}$$

$$h_y = \frac{\int d\Delta y R\,(0, \Delta y))}{R\,(0,0)}$$

Assuming a Gaussian model for the beam profiles, h_x and h_y can then be easily calculated from a Gaussian fit.

However, some words of caution are in order. The bunch intensities are assumed constant in time in the above formalism. In real life this is not the case. Especially, the intensities of the beams decay substantially during a vdM scan. Thus, a time in between the x and y scans is used to measure the bunch intensity decay. Hence, this decay can be corrected. The measured rates have to be corrected for the effects of e.g. pile-up, background and the above mentioned intensity decay. The separations have to be corrected for beam drift and beam-beam deflections. To compute these corrections a first estimation of the reference cross section, using the nominal separations, is needed.

2.5.3 Gain

In detector physics, gain g is describing the ratio of the number of primary ionisation electrons N_0 to the final number of electrons N which is produced in the amplification region (MWPC).

$$g = \frac{N}{N_0}$$

This is an important figure of merit for any amplification process. In the context of this thesis, not the total gain was analysed for each chamber, but the relative gain.

2.5.4 Cosmic muon runs

Some channels have a baseline current under nominal operation. This current offset is intrinsic and a defect of a channel or the power supply, which must be corrected for. In the course of this thesis, measurements of the anode currents taken during cosmic muon runs are used to subtract the offset of the anode currents for each channel. During these runs, one measures the current output of a channel, when almost no particles pass through the chambers (LHC luminosity equals zero).

3 Analysis strategy

In the following chapter, a brief summary of the analysis strategy for this thesis will be given. Each step of the analysis will be described in a dedicated subsection, as different information is used. The coding was the most demanding part of this thesis as no reference code was available. All code was written using the ROOT framework. The entire code can be found on GitHub [18] and easily be extended for further analysis.

3.1 Data sets

For the analysis of the anode currents of the TRD chambers at high luminosity in Run 2 in order evaluate the expected performance in Run 3, data sets from the **D**etector Control System **AR**chive **MA**nager (**DARMA**) were used. The data sets contain voltages, currents, measurement times for both anode and drift channels ranging from the year of installation up to early 2019. These were kindly made accessible by Minjung Kim [19], available under [20]. No measurement uncertainties for these values are available, especially for the anode currents. However, the precision of the current measurements for the drift modules EDS 20 025n_504 is 10 nA and for the anode modules EDS 20 025p_203 is 0.4 nA [10]. Both are three orders of magnitude smaller than the currents seen in this thesis. Henceforth, they are ignored. Measurements of currents and voltages are only taken when a change in value occurs or at a fixed interval. This becomes relevant later on, when combining with other data sets. The data sets are numbered from 1 to 2160. Even though only 522 chambers exist, all 540 possible chambers are considered. Each chamber provides four measurements, the voltage and current for the drift and anode channel. Thus 120 files are assigned to each sector. The first 60 files are for the anode channels and then 60 for the drift channels. The index is incremented first by the layers and then by the stacks. One can deduce the channel from the file index using a channel-mapping file. For example, "sorted_1.csv.root" is assigned to the anode voltage channel of chamber 06_0_0 and "sorted_2.csv.root" to its current channel. File "sorted_3.csv.root" is assigned to the anode voltage channel of chamber 06_0_1. Then later file "sorted_61.csv.root" is assigned to the drift voltage of channel of chamber 06_0_0 and so on.

3.2 Analysis strategy for 2017 luminosity and anode currents correlation

The first high luminosity test was conducted on Monday 4$^{\text{th}}$ September, 2017 in Fill 6168 and Fill 6169 pp collision at $\sqrt{s} = 13$ TeV, details can be accessed under [21]. Additionally a cosmic particle fill on Sunday 3$^{\text{rd}}$ September, 2017 was used to derive the offset current for each channel. Luminosity data is given in this fill by the 0TVX luminosity. Although, the luminosity is not directly available for these data sets, it can be read off from Figure 3.1. This constitutes a major

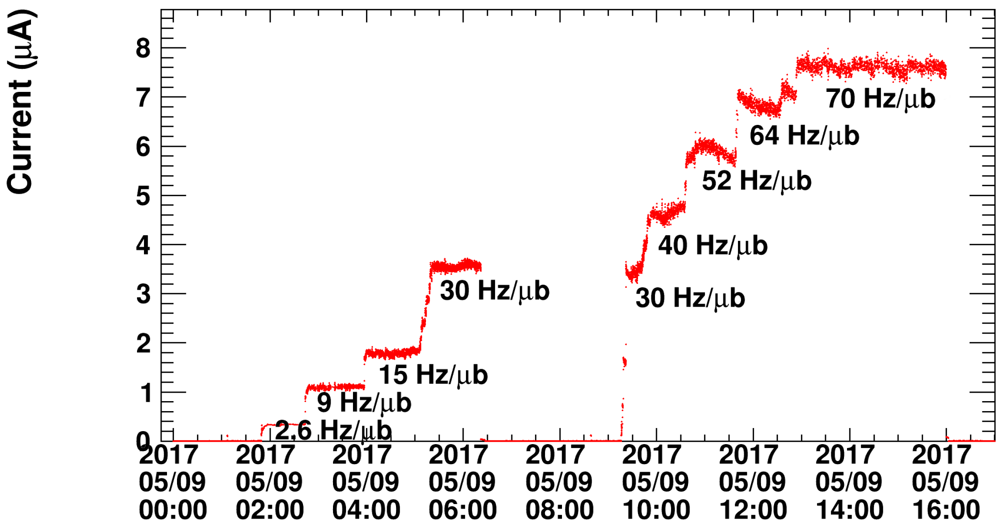

Figure 3.1: Current as a function of time for anode channel 06_0_0A as an example.

downside of these particular data sets since no accurate luminosity data is available, only average values. The highest luminosity step (70 Hz/μb) corresponds to the requirements for Run 3. The operational and defect channels of the ALICE TRD chambers in these data sets are displayed in the appendix in Figure 5.1. A channel is working properly if the the corresponding voltage channel is above 1450 V for the anode channels and above 1900 V for the drift channels. Below these thresholds the channel is working with reduced voltage and for 0 V it is defect. Excellent agreement with the hardware status is formed.

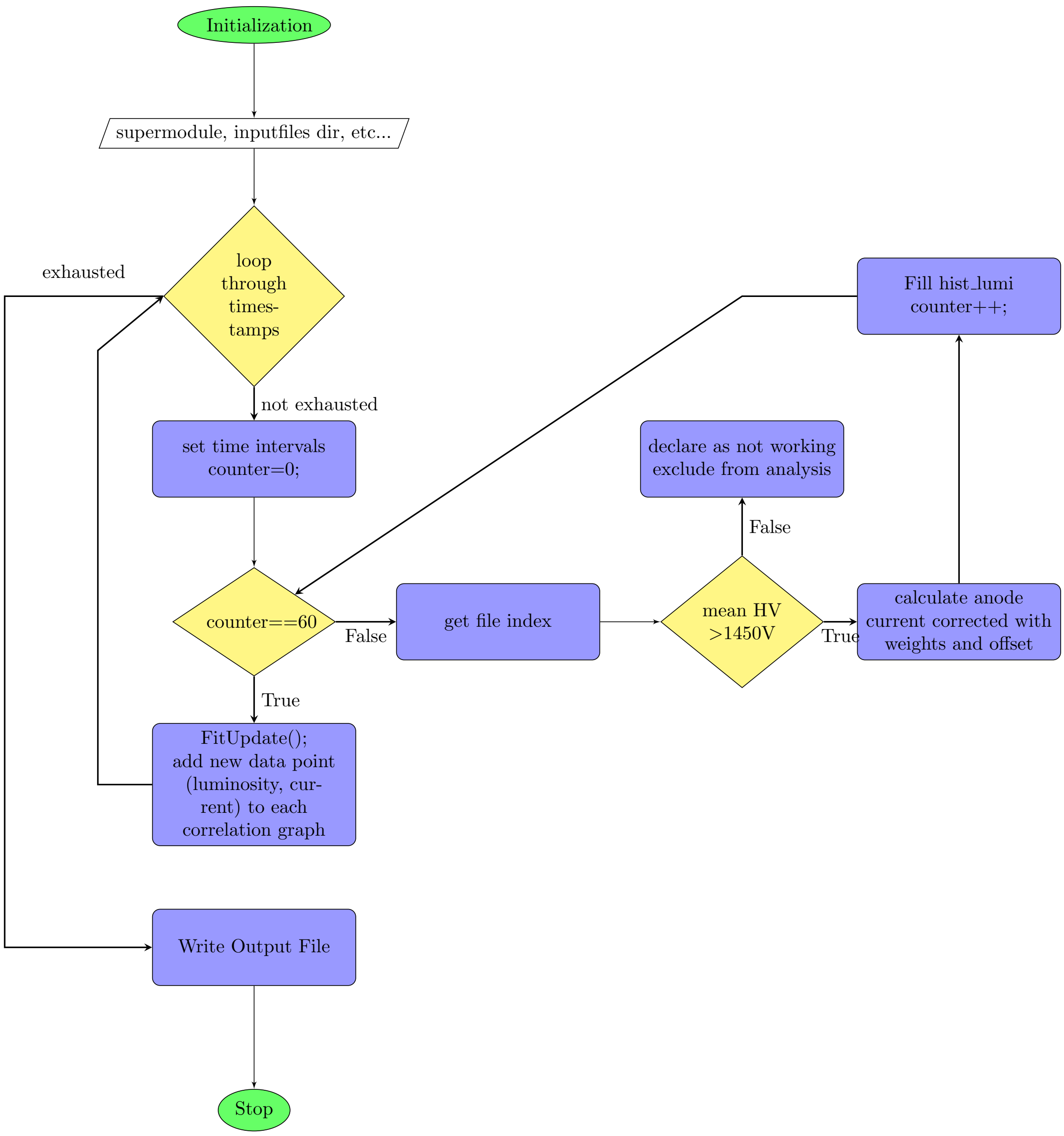

Figure 3.2: Flowchart of the 2017 analysis code to correlate luminosity and anode currents.

With the aid of Figure 3.2 the analysis code to correlate luminosity and anode currents will be explained. Each sector is analysed separately. In order to correlate the TRD anode currents and luminosity, timestamps for the current plateaus are read off from Figure 3.1 forming time intervals to loop through. A counter is introduced for convenience to only iterate through the necessary 60 files, which contain the anode currents and voltages. Then the needed file index is read from the channel-mapping-file. The average voltage is determined for each time interval corresponding to each luminosity step. If the average voltage exceeds the preset threshold of 1450 V, the chamber works properly throughout the interval and one proceeds to calculate the corrected anode current. The corrected anode current is the average current for each step multiplied by a weight. The weight represents a correction due to the differences between the chambers. The weights are thoroughly discussed in Section 4.1. If the channel does not meet this criterium, it is declared as not working or working with reduced voltage and excluded from further analysis. Then a histogram containing the average currents for each luminosity step of each channel in a sector is filled. Next, a graph for each channel containing the average current for each luminosity step is fitted with a linear model. If all timestamps were seen, an output file is written. The results are presented in Section 4.1.

3.3 Analysis strategy for 2018 luminosity and anode currents correlation

Proton-proton collisions at $\sqrt{s} = 13$ TeV in Fill 7122 on Monday 3$^{\text{rd}}$ September, 2018, Fill 7133 and Fill 7135 on Friday 7$^{\text{th}}$ September, 2018, taken in the morning and in the afternoon, were analysed to correlate luminosity and anode currents. Likewise to 2017, a cosmic muon run on Wednesday 22$^{\text{nd}}$ August, 2018 is used in order to derive an offset current for each channel. The active chambers of the ALICE TRD chambers are displayed in Figure 5.2, which comparatively to Figure 5.1 had become worse. For this data set, the measurements from the EMCal detector provide a higher granularity in luminosity data. However, since data taking does not happen concurrently, one has to align the measurements of the EMCal detector with the anode current measurements in time. A flowchart for the alignment can be found in Figure 3.3.

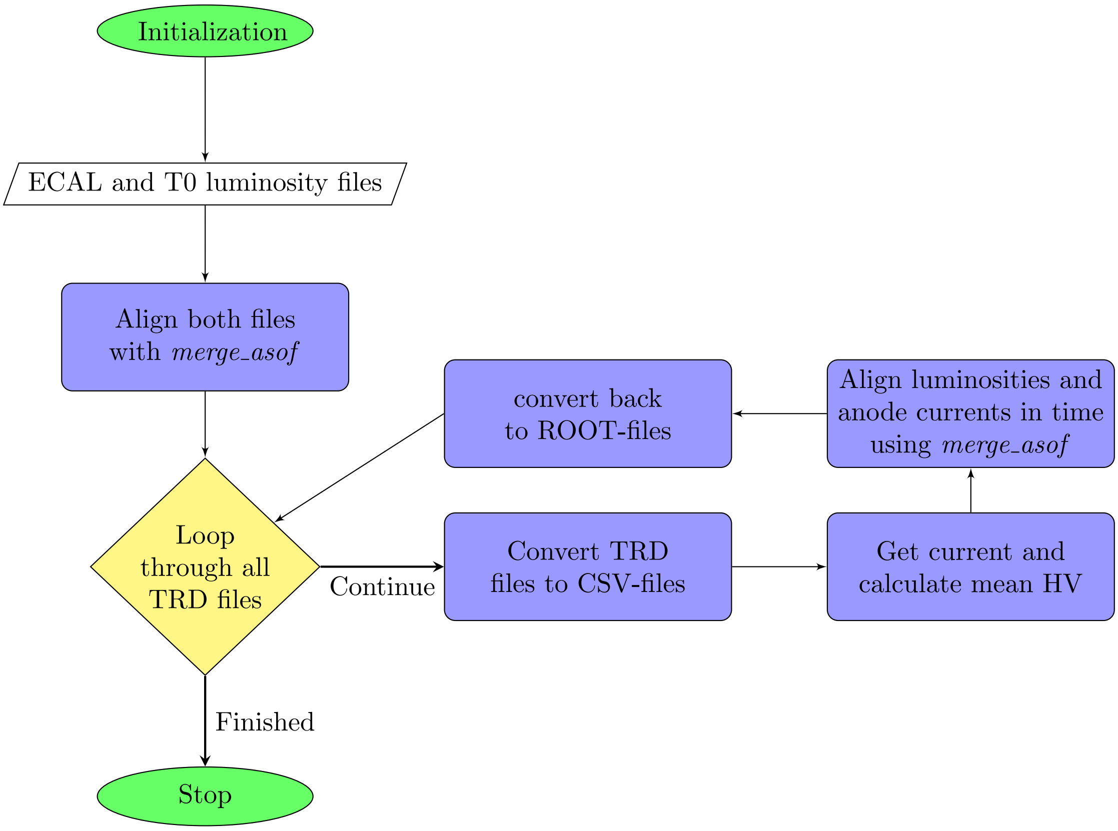

Figure 3.3: Flowchart of the alignment code for EMCAL detector luminosity with current measurements used in the 2018 analysis code.

Specifically, one had to look into five second intervals for data points in the measurements of the EMCal detector luminosity and anode current data sets and match them. The above fills were extracted into a CSV-file and aligned using the provided *merge_ asof* function by the python pandas module with the *nearest* option. Then the code looped through all TRD files and converted them to CSV-files. Subsequentially, an average voltage was calculated in these five second intervals and the luminosities and anode currents were aligned, again with the *merge_ asof* function. In the end, all the files were converted back to ROOT-files.

Besides that, the year 2018 is analysed analogous to the year 2017. The flowchart is shown in Figure 3.4.

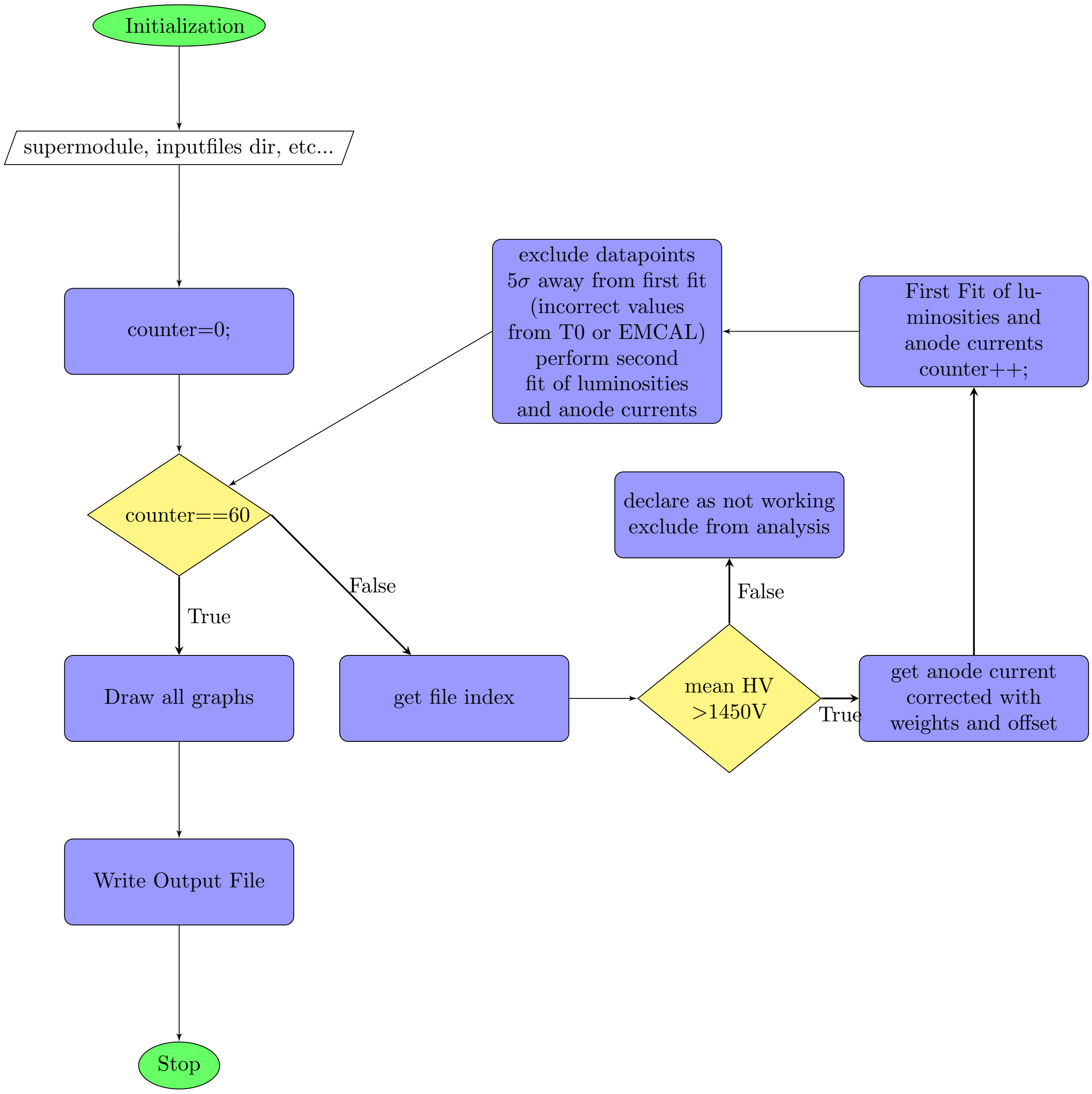

Figure 3.4: Flowchart for 2018 analysis code to correlate luminosity and anode currents.

In contrast to 2017, one does not have to loop through time intervals and can directly fit the dependence of luminosity and anode currents. In order to minimize false measurements from the EMCal detector affecting the fit results, a first fit is performed, then all data points which are more than 5σ away are excluded and a second fit is performed. The results are presented in Section 4.2.

3.4 Chaotic current detection

Some anode channels randomly show a chaotic current (see Figure 3.5) before exceeding a preset threshold and initiating the secure shutdown procedures. It was found afterwards, that predominately the 4.7 nF and 2.2 nF capacitors in the resistor chain for the power supply seemingly failed. Only a weak correlation (low statistics) with the operating time of each chamber was found. Thus the chambers can be put into groups with and without the previously alluded to capacitors.

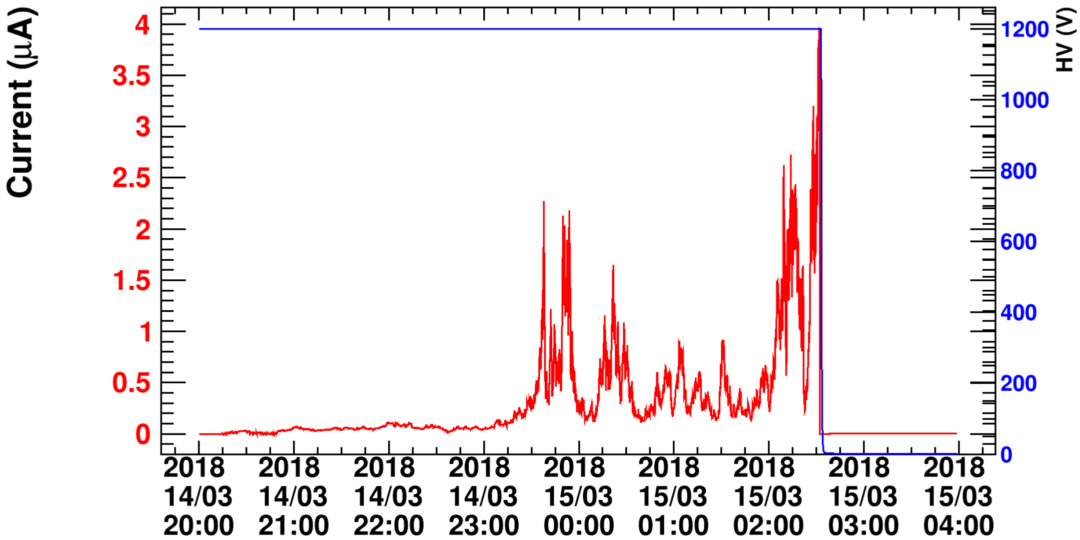

Figure 3.5: This chamber already exhibits a chaotic current at reduced voltage (nominal voltage 1530 V), other chambers show a constant current equal to zero at low luminosities.

In order to avoid that such currents disturb measurements, the plan is to detect these chambers early on. One can then operate them with a reduced voltage, prolonging the chamber's lifetime. Consequently, an automatic detection scheme needs to be implemented as to avoid manually monitoring the currents of 522 chambers. To detect this chaotic current on the fly, an adaptation of the smoothed z-score algorithm, presented in [22], was implemented. The algorithm was chosen for its simplicity, minimal memory usage and low computation complexity. With the aid of Figure 3.6, the detection scheme will be presented.

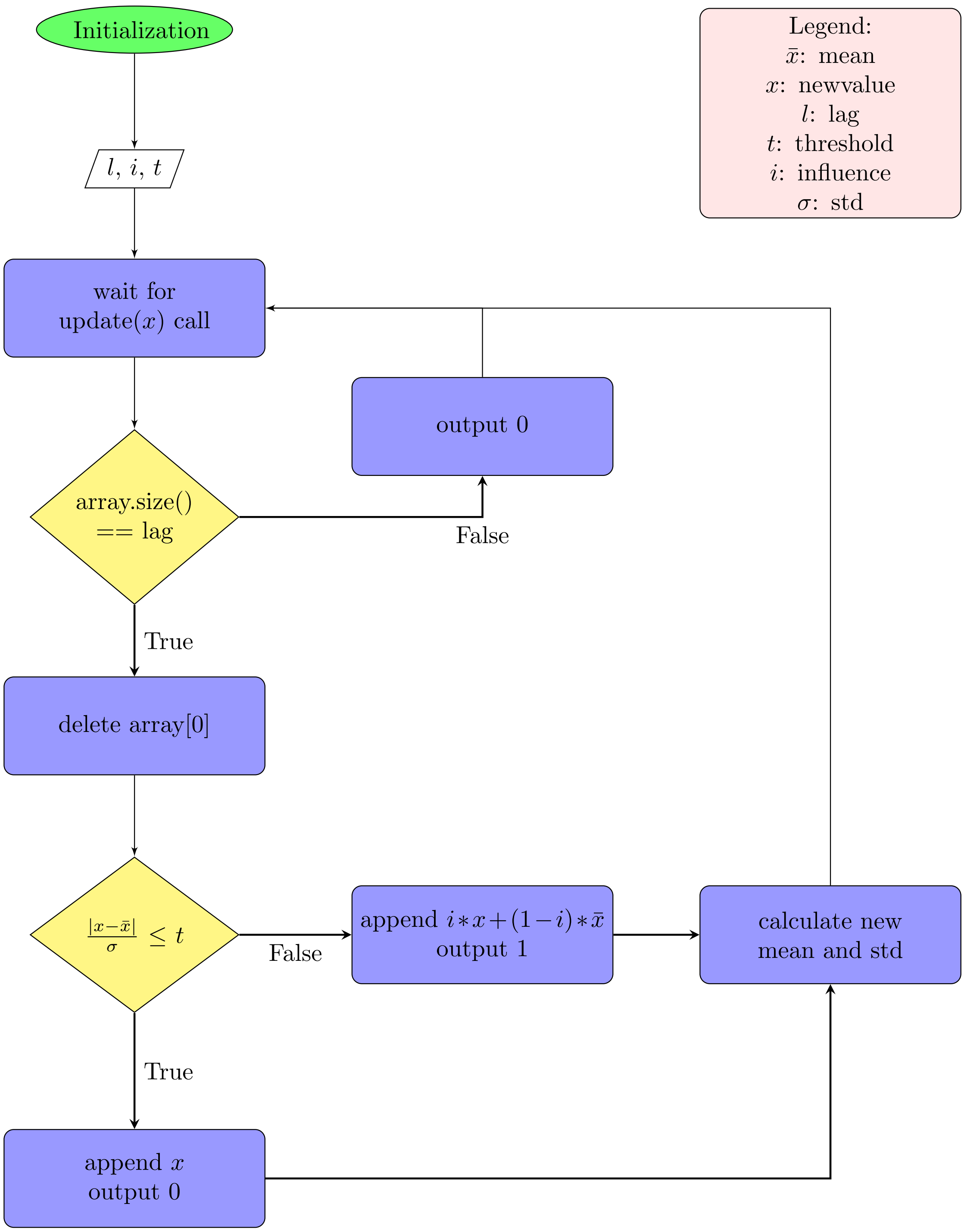

Figure 3.6: Flowchart of the chaotic current detection algorithm.

To initialize the class *lag*, *threshold* and *influence* need to be specified. It is then designed to take a data point and determine whether the given value is an outlier, defining a *signal*, indicating that something has possibly gone wrong. When given a new data point, the algorithm compares the new data point by computing the number of standard deviations (z-score) the new data point lies away from the moving mean (where the length of the moving mean is controlled by *lag*). This defines the z-score of the new data point. If this z-score exceeds a preset *threshold*, then the new point is declared to be a *signal*. This is first done, when the array is completely filled in order to avoid that low statistics affect the output. When the array is full, the first element will be deleted to make room for the new value. To ensure that a *signal* does not prevent future *signals* from triggering, when computing the new moving mean and moving standard deviation, a filtered value of the *signal* is used instead. Specifically, the filtered value is a scaled combination of the current *signal* and the previous moving mean, where the scaling is controlled by the *influence* parameter. In the end, the algorithm always waits for a new data point. The whole code is packaged into a class and ready for use, however implementation may be altered for real life use. The results of this algorithm and its performance on the parameters are presented in Section 4.3.

3.5 Van der Meer scans

The data sets providing the V0 rates are available under [23]. Here, Fill 6012 pp collision at $\sqrt{s} = 13$ TeV was analysed. A similar alignment as described in the preceding sections had to be performed on these data sets. A flowchart is displayed in Figure 3.7.

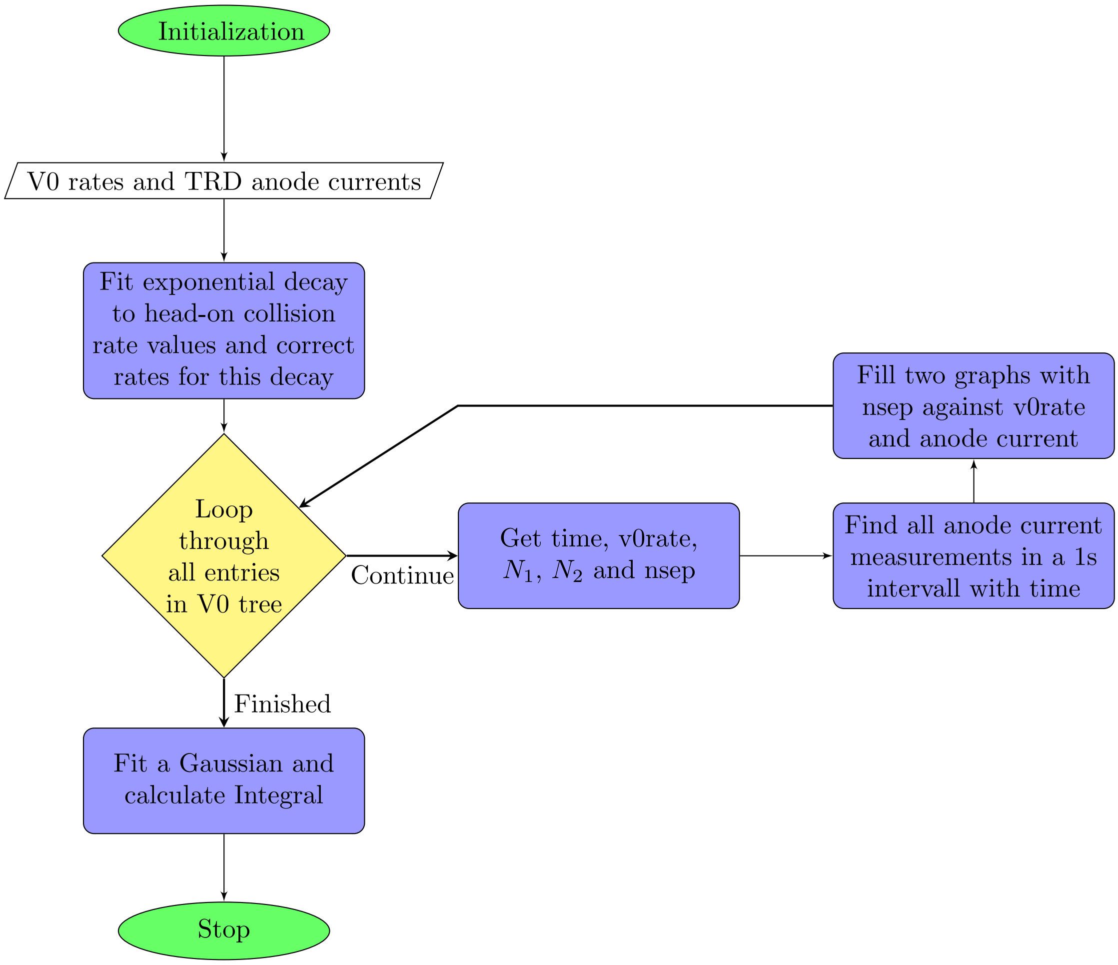

Figure 3.7: Flowchart to align V0 rates and anode currents.

In the first iteration the values for head-on collisions are fitted by an exponential decay model in order to account for the bunch intensity decay. This model is then used to correct the rates for this exponential decay. Subsequently, all entries in the V0 rates file are iterated through a second time, extracting rate, intensities, time and nominal separation of the beams, given in mm. Then for each entry all measured currents in a 1 s interval are plotted. When completed, a Gaussian is fitted to the rate against the nominal separation. From the Gaussian, the integral and the maximum are calculated. This suffices for all further calculations. As an example, chamber 06_0_0 was chosen arbitrarily as it is known to be working properly.

4 Results

As explained in Section 1.2, a thorough understanding of the anode currents of the ALICE TRD is essential for the successful operation of the detector in Run 3. In this chapter the dependences of anode current and luminosity will be determined and examined.

Firstly, the results from tests in Run 2 in 2017, where one used the same luminosity expected in Run 3, will be presented in Section 4.1.

Secondly, similar tests in Run 2 in 2018 will be analysed in Section 4.2. Here, a more in depth analysis is possible due to the usage of more precise measurements for the luminosity. Additionally, a shallow analysis of parameters like the gas-mixture and pressure will be presented.

Thirdly, the results from using a simple algorithm with a z-score for chaotic current detection will be presented in Section 4.3.

Lastly, in Section 4.4 a value for the cross section will be calculated using only anode currents of the TRD recorded during a van der Meer scan.

4.1 Results from 2017

As a first step, the dependence of anode currents of all supermodules on luminosity was studied. To ensure that outliers were negligible, the anode currents were binned and averaged over the luminosity bins, shown in Figure 3.1. The details of the algorithm are described in Section 3.2. The standard deviation of the averaging procedure was used as the measurement uncertainty. An example for one supermodule can be found in Figure 4.1.

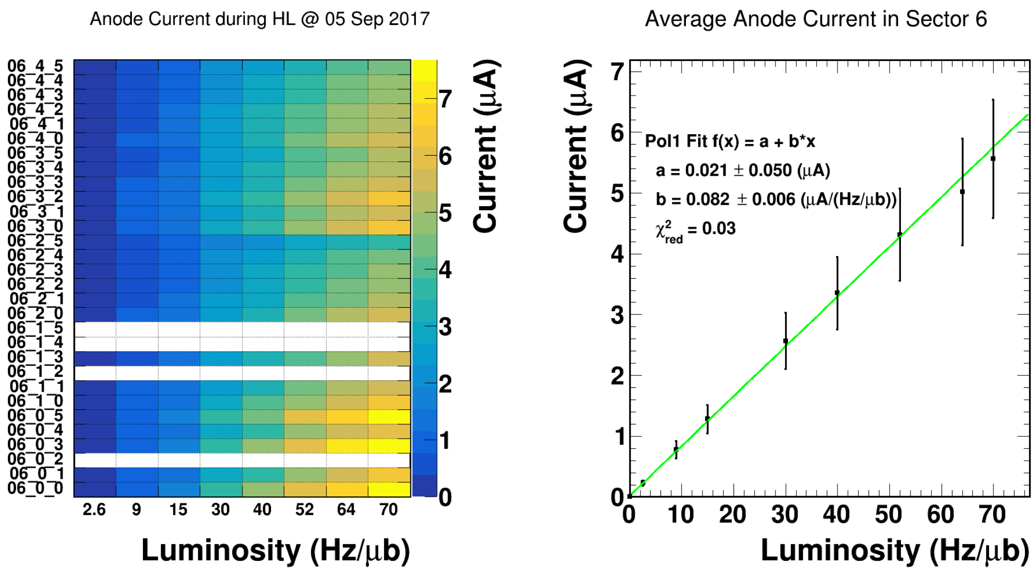

Figure 4.1: On the left side, the average currents of all chambers in sector 6 for various luminosities are shown. Non-functioning chambers appear white. No weights are applied. On the right side, the average anode current of all working chambers in this sector against the luminosity with a linear fit is shown.

From Figure 4.1 one can deduce a couple of things. Namely, that the position of the chamber has a strong correlation to the produced current. This is to be expected, since chambers positioned close to the collision point (lower layer) will see more particles and produce more current. Not only differences in layers are expected, but also in the stacks itself. Stack 0 will produce higher currents due to it closeness to the metal door of the ALICE solenoid magnet, where additional particles are scattered and a larger current is thus produced. The same reasoning would apply to stack 4, but stack 4 is shielded by the muon absorber, blocking some particles from reaching this stack. Stack 1 and 3 behave similar and produce a higher current than stack 2 as the chamber covers a larger solid angle. This is all visible on the left side of Figure 4.1. The right-hand side of Figure 4.1 is already very indicative of a clear linear dependency of current and luminosity. The error-bars of currents at higher luminosities are large, this however stems from the previously mentioned positional dependence of the TRD chambers.

For the fit a first order polynomial function was used: $f(x) = a + b \cdot x$. A single fit for one chamber can be found in Figure 4.2. One can see, a very nice linear correlation of the luminosity and anode current. The large χ^2_{red} was attributed to the imprecise luminosity values. No indication of a higher order correlation was found. A complete set of fits for a sector can be found in the appendix in Figure 5.3.

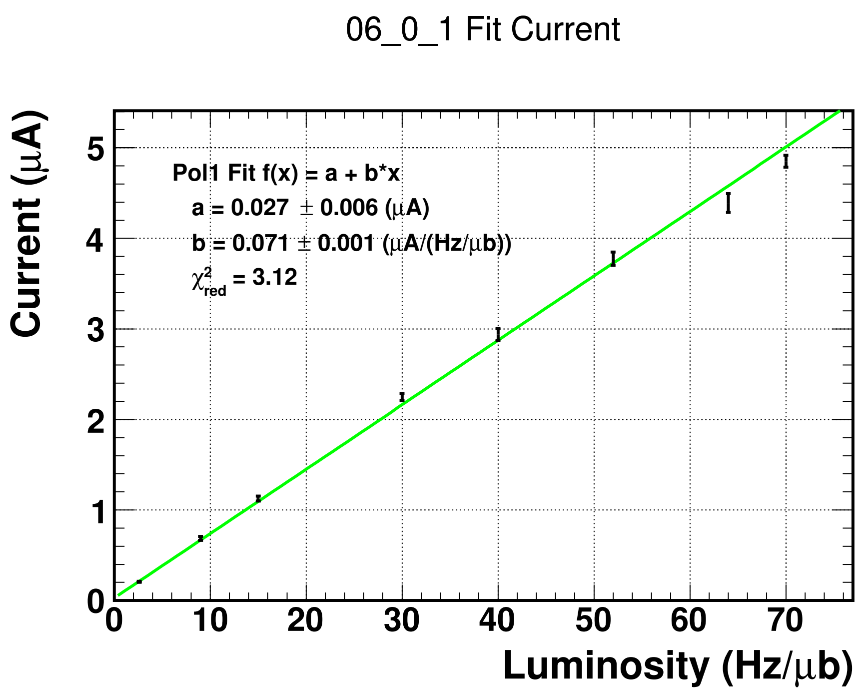

Figure 4.2: Example fit for chamber 06_0_1.

In the next step of the analysis, the above fit procedure for a single chamber was repeated for every chamber to look at the distribution of the slope parameter (b). The offset parameter (a) was also studied but did not follow any discernable distribution. This was to be expected, since the offset of every chamber was corrected for with cosmic muon runs, see Section 3.2.

Here, one must describe the weights applied to the anode currents. A multitude of weights were considered to account for difference in size, gain, voltage, full solid angle coverage and position, but in the end only two were used, as these proved to be most effective.

The first reasonable weight was used to account for the differently sized chambers in Table

2.1. Larger chambers produce a higher anode current than smaller ones due to a larger area for particles to interact with. This was corrected for by dividing the active area of a chamber by the smallest one in the sector, thus ensuring a vanishing size dependence. The different distributions of the slope parameters are displayed in Figure 4.3.

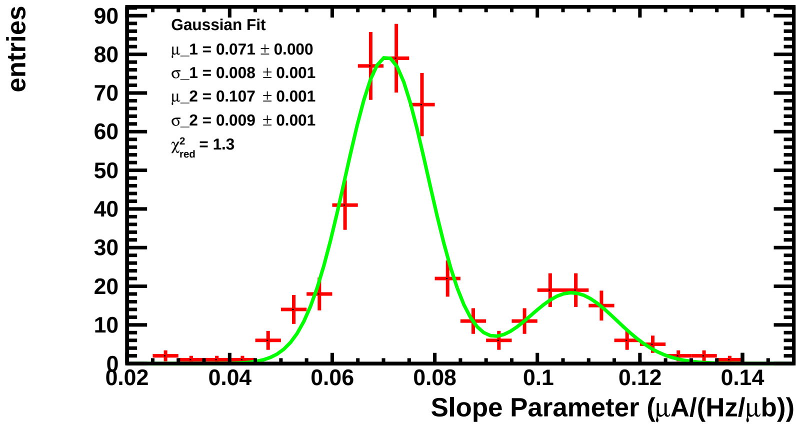

(a) before.

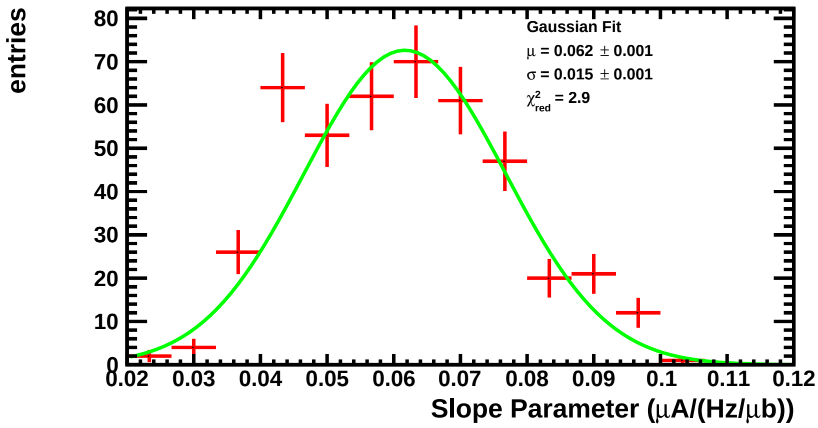

(b) after.

Figure 4.3: Distribution of slope parameter before and after accounting for the different chamber sizes.

Without any weights, a distribution with two distinct peaks is visible in Figure 4.3a. The second peak contains the higher slope parameters from stack 0, due to its position near the metal door. The first peak contains the slope parameters from all other stacks. After applying a correction for the chamber size, the double Gaussian reduced to a broader single peak plateau, see Figure 4.3b.

The second weight is used to account for for differences in full solid angle coverage. Smaller coverage results in less current being produced, as fewer particles are detected by the chamber. To correct for the decreasing coverage in radial direction, the chamber size increases radially. Thus in a stack all chambers cover roughly the same angle, except for chambers in stack 2 as the chamber size does not increase radially. The full solid angle coverage for each chamber in a sector was calculated and is presented in Table 2.2. A vanishing full solid angle coverage dependence was achieved by dividing the solid angle for each chamber by the solid angle of the smallest chamber.

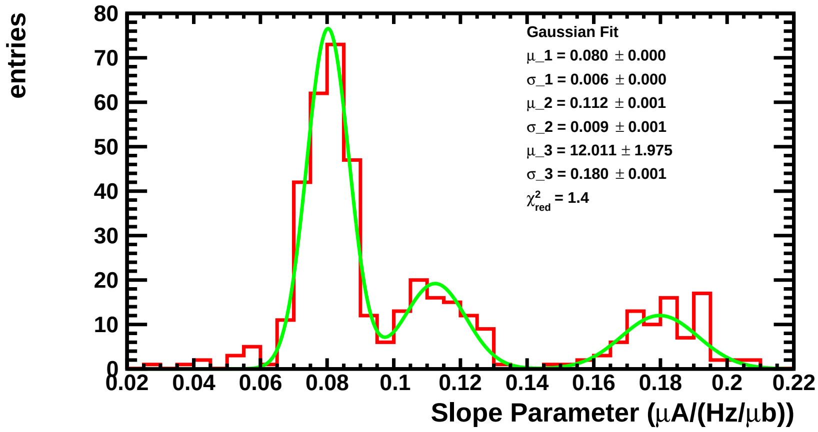

Figure 4.4: Distribution of slope parameter after applying the weight for different solid angle coverage of each chamber.

This weight changed the overall distribution quite a lot when comparing Figure 4.4 and Figure 4.3a. A third peak appears for higher slope parameter. It was shown that the first peak come from stack 1-3, the second to stack 4 and the third peak to stack 0. Additionally, this weight made the distribution on a stack level quite homogenous, see below.

These two weights must not be combined. The increasing chamber size is exactly to account for different full solid angle coverage of a chamber in radial direction. Thus, combining the weights leads to a double correction.

The next weight considered a difference in gain as a reason for different anode currents.

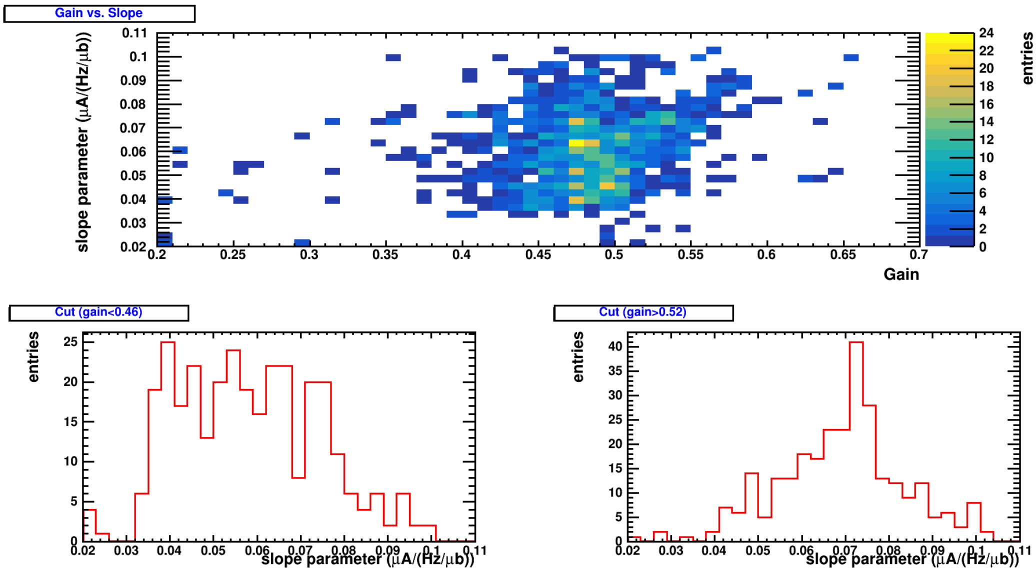

Figure 4.5: The upper plot shows the correlation of gain on the slope parameter. The lower plots show the projection on the slope parameter for two different cuts. The chamber size as a weight was applied.

One can see in Figure 4.5 that no clear correlation is visible. Furthermore, in the appendix in Section 5 all plots above are shown with the gain as a weight. These show no clear improvement or difference. Henceforth, the gain as a weight was abandoned. Also, no improvement was achieved by combining the gain and the chamber size as a weight.

Another possible weight could be the applied voltage. However, since the voltage is specifically calibrated for each chamber in order to make the gain uniform, a weight in voltage would be counter-acting this procedure. There is no reasonable way to account for chambers working with reduced voltage, hence they were completely excluded.

The last weight that was considered was a positional weight of the the chambers to account for the positional dependence, since lower layers produce more current. However for the purpose of this thesis, the positional dependence was desirable and hence this weight was not studied further.

As it depends on what one would like to investigate, both weights (chamber size and full solid angle coverage) will be presented.

Turning back to the analysis, one expected the distribution of the slope parameter to have a mean value close to the slope parameter found in Figure 4.1. Although limited due to the low number of counts, only 522 chambers minus the not working ones, different distributions for the two weights were observed in Figure 4.3b and in Figure 4.4.

As a first step, to approximate the mean of the distributions, Gaussians were fitted. To understand the width of the distributions, a differential analysis was conducted. Specifically, subdividing the slope parameter firstly into the different stacks and secondly into layers.

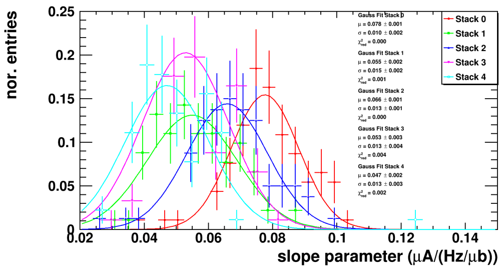

(a) Chamber size as weight.

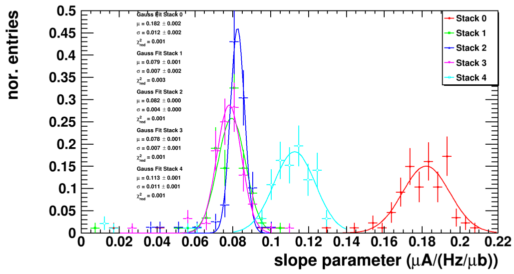

(b) Full solid angle coverage as weight.

Figure 4.6: Slope parameter of the different stacks. Each histogram of the different stacks is normalized to its area in order to account for the not working chambers.

This is shown in Figure 4.6. It was found that the various Gaussian fits either do not appropriately describe the underlying model or due to low number of counts are not able to. This effect is enhanced in Figure 4.6a than in Figure 4.6b. Nonetheless, a clear positional dependence of the slope is visible for both.

In order to understand the width of the distribution, i.e. study the layer dependence, stack 1 and stack 3 were combined, as they behave very similar. As already explained, the slope parameter in the lower layers should be considerably higher than in the upper layers. In [24] it was simulated that the relative number of charged particles entering and leaving the TRD is roughly 1.6. Thus one expected a clear separation into ascending layer order and a similar factor when comparing mean currents of layer 0 and layer 5.

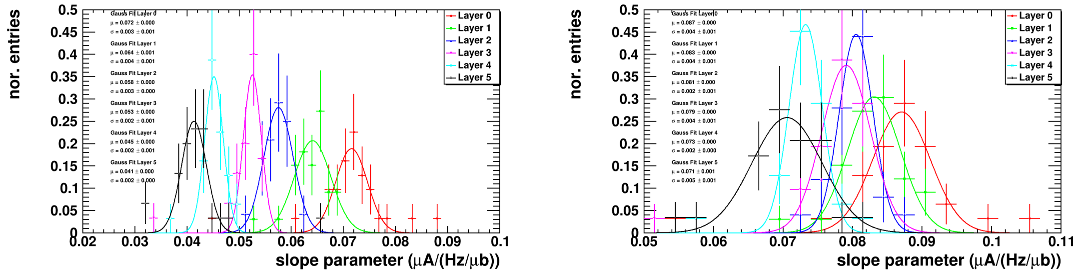

(a) Chamber size as weight.

(b) Full solid angle coverage as weight.

Figure 4.7: Slope parameter of the different layers in stacks 1 and 3. Each histogram of the different layers is normalized to its area in order to account for the not working chambers.

Figure 4.7 confirms exactly what was postulated above for both weights. The ascending order and a very clear separation are visible in Figure 4.7a. A similar ordering is visible in Figure 4.7b, though not as clearly. The relative means of the fit from layer 0 and layer 5 are 1.76 ± 0.07 in Figure 4.7a and 1.23 ± 0.10 in Figure 4.7b, thus confirming the simulated factor given in [24].

The last point was to look at an η-ϕ map. The ϕ-direction gives the dependence of the slope parameter as a function of layer. The η-direction shows the distribution of the slope parameter as a function of stack. For this, all calculated slope parameters in a given stack or layer are averaged, respectively, and displayed in Figure 4.8.

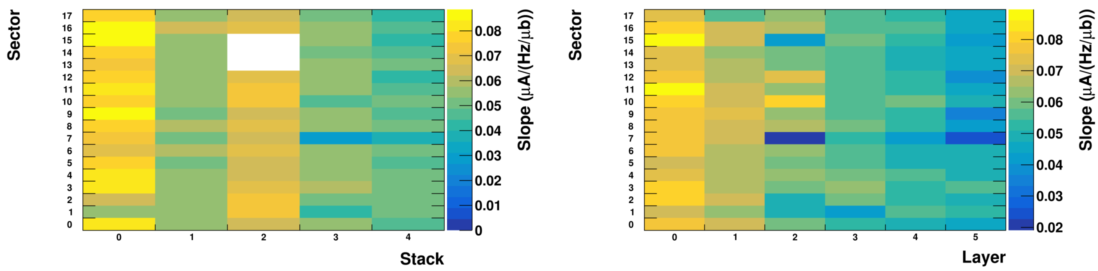

(a) Slope parameter vs stack.

(b) Slope parameter vs layer.

Figure 4.8: η-ϕ map with chamber size as weight.

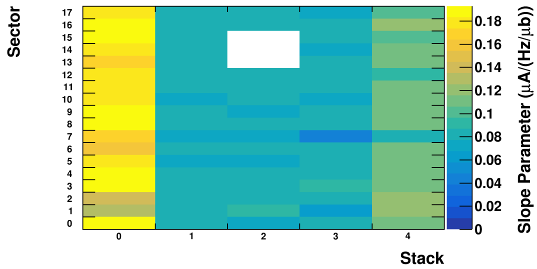

(a) Slope parameter vs stack.

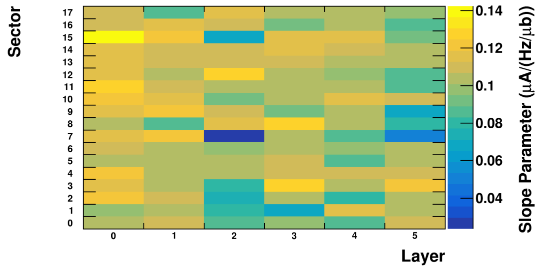

(b) Slope parameter vs layer.

Figure 4.9: η-ϕ map with full solid angle coverage as weight.

The stacks in Figure 4.8a behaved exactly as one would expect. Stack 0 and 4 are close to the metal wall, where additional particles are scattered, but in front of stack 4 the muon absorber is located, reducing the slope parameter. Stack 1−3 behave roughly similar, although the values in stack 2 are bit higher. The outliers can be explained with Figure 5.1 (appendix) in the following way: in a stack, if chambers in lower layers do not function, the average slope parameter is smaller. An example of this are the outliers in stack 0 and sector 1. Comparing which chambers are fully operational (see in the appendix in Figure 5.1). Only the first, fourth and fifth layers were actually working. Hence, the average fit parameter is comparatively smaller than a fully operational stack. As expected, the η map in Figure 4.8b shows a radial dependence. Inner layers produce higher currents than outer ones. This is due to the decreasing number of particles, see [24]. The outliers in this figure exist for the same reasons as in Figure 4.8a.

In Figure 4.9a it can be seen, that the full solid angle coverage weight made the stacks 1−3 very homogenous. The radial dependence vanished in Figure 4.9b.

4.2 Results from 2018

As already stated in Section 3.3,the 2018 data sets are analysed analogous to the ones in 2017. However, the previous analysis method was refined to incorporate luminosity measurements of the EMCal detector. Henceforth, only the weight for the chamber size was used. The details of the algorithm is described in Section 3.3. The results are displayed in Figure 4.10.

A clear correlation in all three separate measurements was visible, further confirming a linear model. Additionally, it is remarkable that even up to 120 $Hz/\mu b$, which is more than double the design specifications for Run 3, the linear model applies and the currents continue to be stable. Generally, the detector showed a stable performance and reproducibility in these tests. In Figure 4.10c one can see that the LHC team three times shortly overshot manually dialling in the specified luminosity.

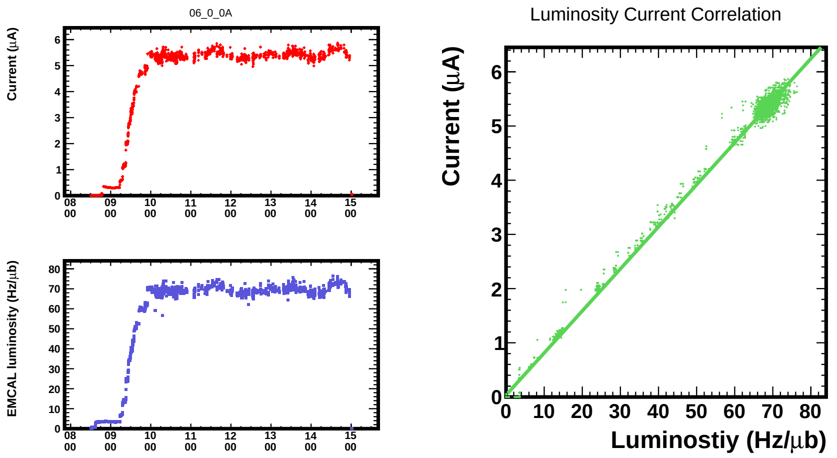

(a) High luminosity measurement in Fill 7122 pp collision at $\sqrt{s} = 13$ TeV.

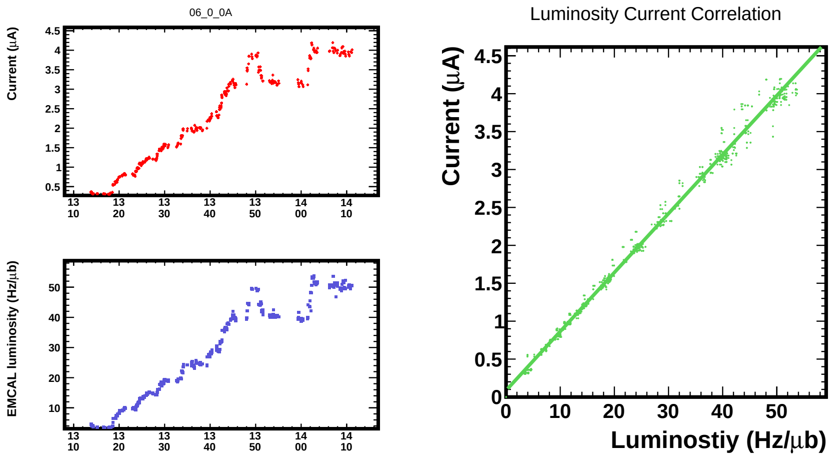

(b) High luminosity measurement in Fill 7133 pp collision at $\sqrt{s} = 13$ TeV.

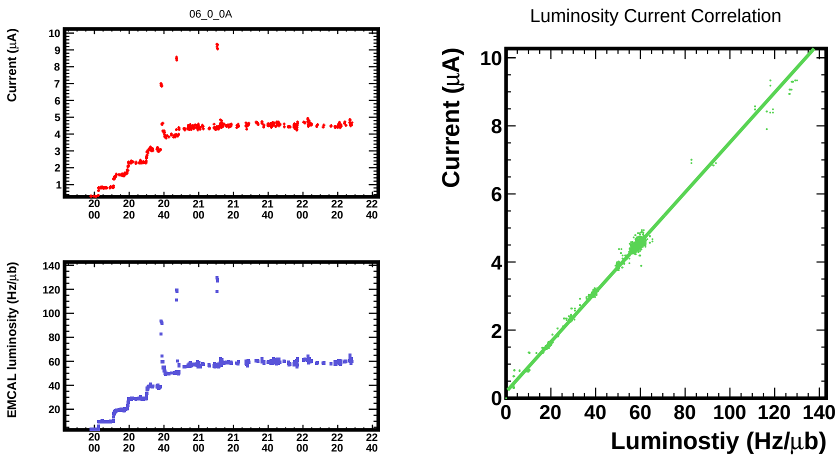

(c) High luminosity measurement in Fill 7135 pp collision at $\sqrt{s} = 13$ TeV.

Figure 4.10: 2018 luminosity measurements. On the left side, the luminosity and current are shown against time. On the right side, the luminosity vs the current for the single chamber is plotted.

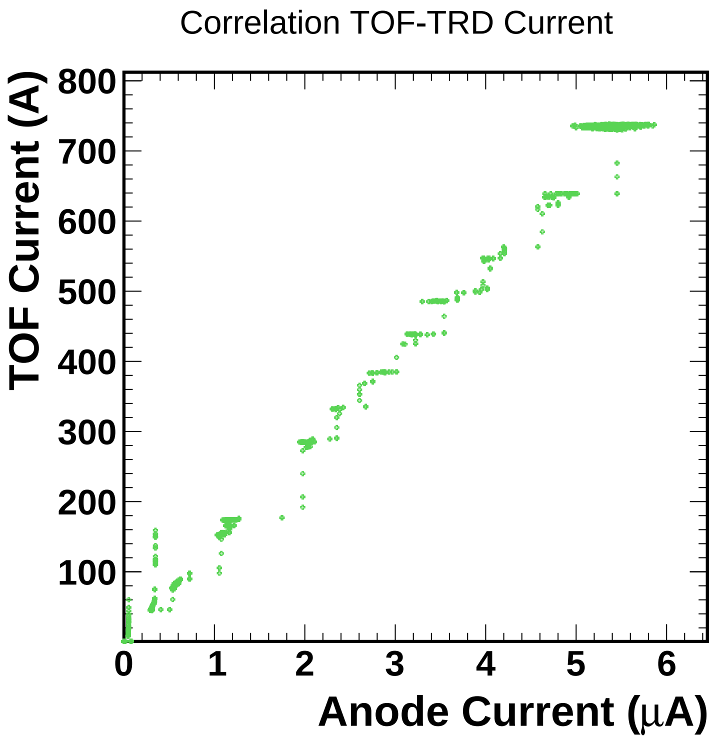

Figure 4.11: Correlation of TOF and TRD currents.

From Figure 4.11 one can deduce that the TOF and TRD currents are correlated. The stepwise distribution of points originates from the alignment in time method used. A fit for a single chamber for each fill is shown in the appendix in Figure 5.5. The distribution of the slope parameter can be found in the appendix in Figure 5.6.

More light will now be shed on the individual differences between the three measurements. This is done by looking at the slope parameter at layer level of stack 1 and 3, much in the same way as in Figure 4.7a. This will allow one to gain further insight on the importance of internal parameters like the gas-mixture and external ones like pressure and temperature.

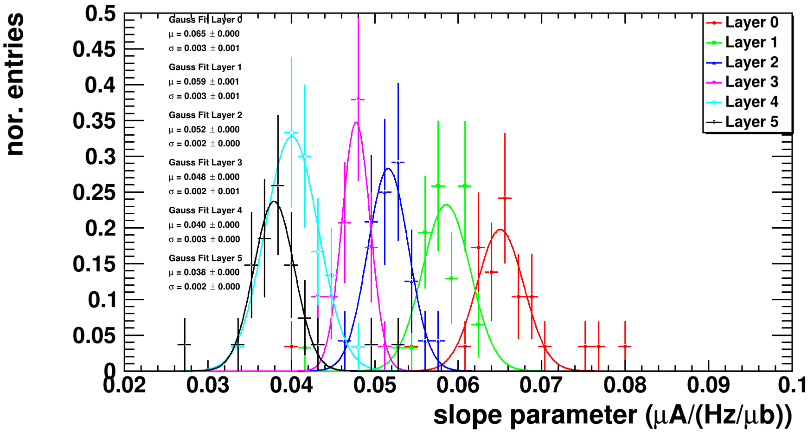

(a) Slope parameter in Fill 7122.

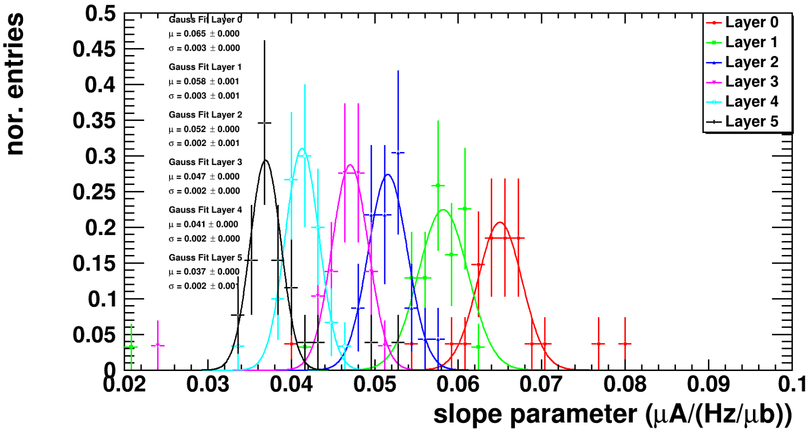

(b) Slope parameter in Fill 7133.

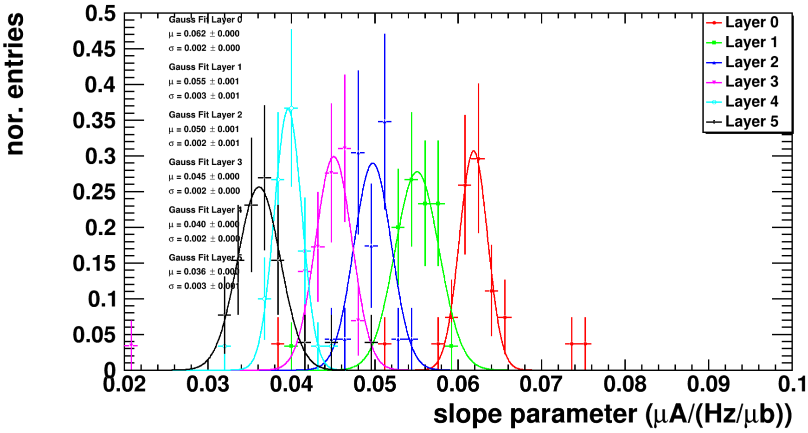

(c) Slope parameter in Fill 7135.

Figure 4.12: 2018 slope parameters at layer level.

The results in Figure 4.12a and in Figure 4.12b are consistent. The fit results are shown in Table 4.1. The results deviate little from the ones obtained from Figure 4.7a. The variation can be mainly attributed to the luminosity values not being precise in the measurement of 2017. This shows, that the slope parameter of the ALICE TRD currents are consistent and stable over multiple days.

Gaussian Fit of	Fill 7122	Fill 7133	Fill 7135
Layer 0			
$\mu =$	0.065 ± 0.000	0.065 ± 0.000	0.062 ± 0.000
$\sigma =$	0.003 ± 0.001	0.003 ± 0.000	0.002 ± 0.000
Layer 1			
$\mu =$	0.059 ± 0.001	0.058 ± 0.001	0.053 ± 0.001
$\sigma =$	0.003 ± 0.001	0.003 ± 0.001	0.003 ± 0.001
Layer 2			
$\mu =$	0.052 ± 0.000	0.052 ± 0.000	0.050 ± 0.001
$\sigma =$	0.002 ± 0.000	0.002 ± 0.001	0.002 ± 0.001
Layer 3			
$\mu =$	0.048 ± 0.000	0.047 ± 0.000	0.045 ± 0.000
$\sigma =$	0.002 ± 0.001	0.002 ± 0.000	0.002 ± 0.000
Layer 4			
$\mu =$	0.040 ± 0.000	0.041 ± 0.000	0.040 ± 0.000
$\sigma =$	0.003 ± 0.001	0.002 ± 0.000	0.002 ± 0.000
Layer 5			
$\mu =$	0.038 ± 0.000	0.037 ± 0.000	0.036 ± 0.000
$\sigma =$	0.002 ± 0.000	0.002 ± 0.001	0.003 ± 0.001

Table 4.1: Fit results from Figure 4.12 in pp collisions at $\sqrt{s} = 13$ TeV.

In Figure 4.13, the radial position of the middle of the pad-plane was plotted against the slope parameters. The values are obtained from the mean and for the uncertainties the standard deviations from Fill 7133 were taken. As expected, a linear correlation of the pad-plane position and the slope parameter was observed.

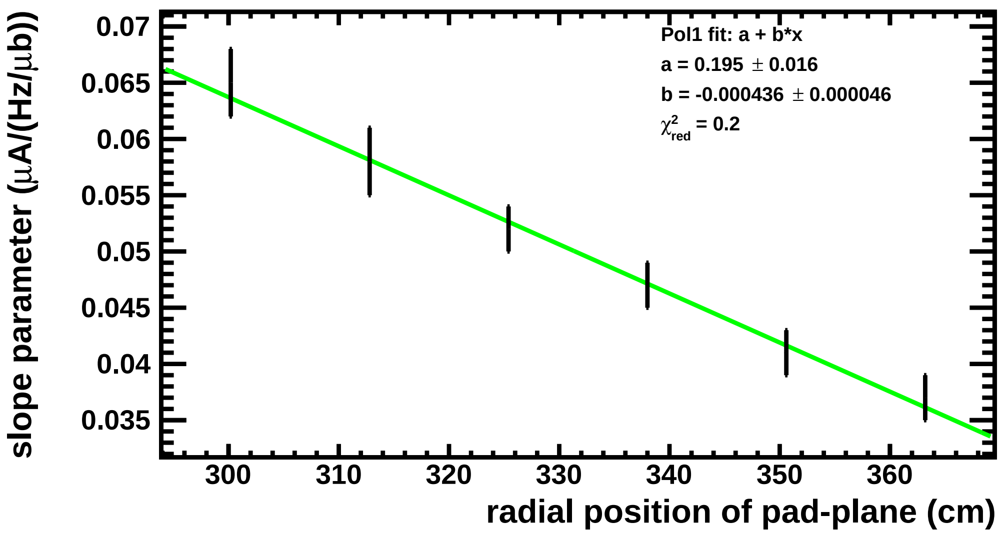

Figure 4.13: Position of the chamber against the mean value in Figure 4.12b, showing a clear expected radial dependency.

Although the results from the different measurements agree within uncertainty, a closer look must be paid to the trend emerging in Figure 4.12c. Here, all fit results are decreased by an offset. However, the results only deviate very slightly so this could also just be random fluctuation within the measurement uncertainty. One would postulate that since both measurements were taken on the very same day, both would produce the same results. This however is not the case. The source of this deviation can stem from both external factors, like pressure and temperature, but also from internal ones, like the gas mixture. In the following, both will be examined.

A thorough investigation into the pressure dependence of the gain had already been conducted by [13]. There, a definite anti-correlation of gain and pressure was found. Higher pressure results in a lower gain and thus in a lower anode current.

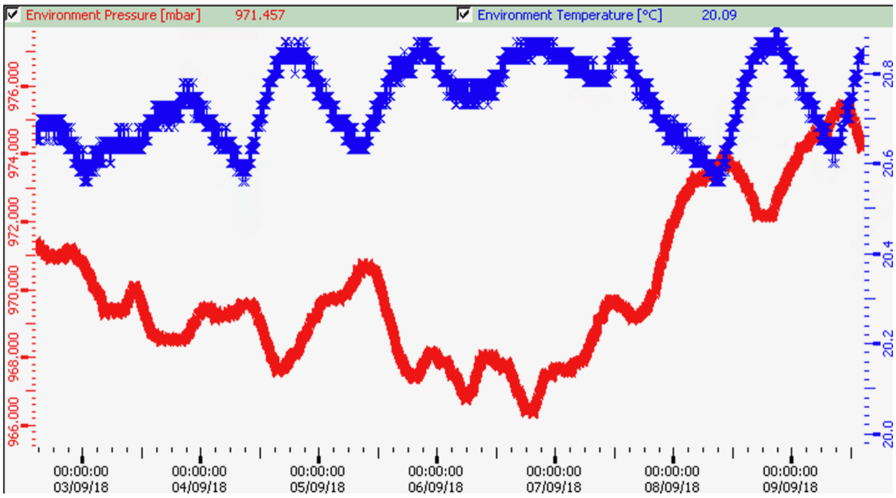

Figure 4.14: Temperature and pressure.

In Figure 4.14, the atmospheric pressure and temperature inside the ALICE chamber is displayed. The atmospheric pressure is directly correlated to the internal gas pressure in a TRD chamber, as is the temperature. One can clearly see, that on Friday 7$^{\text{th}}$ September, 2018 the pressure rose significantly over the course of the day, while temperature remained largely steady. Therefore, according to [13], a higher gain is seen in the morning, while a lower gain is observed in the afternoon. This fact contributed irrefutably to the higher slope parameters in the morning, while having lower slope parameters in the afternoon.

As pointed out by [13], the gain decreases by 4.2% for each percent N_2 added. However, the gas mixture only changes slowly, as can be seen in the appendix in Figure 5.7b, the N_2 content decreased only very slightly over the day. The contamination by water (in the appendix in Figure 5.7a) and oxygen (in the appendix in Figure 5.7c) remained largely steady over the day.

Hence, pressure is the biggest influence for this slight difference of measurements within uncertainty in Fill 7133 and Fill 7135 in pp collisions at $\sqrt{s} = 13$ TeV. This is easily correctable in future data sets.

4.3 Chaotic current detection

In the following, the algorithm, explained in Section 3.4, is tested. The objective, here, is to minimize the *signal* output for a known working reference chamber, while maximizing *signal* output for a chamber exhibiting these currents. Additionally, one needed to take into account that a change in luminosity causes a change in anode currents, as shown in Section 4.1 and Section 4.2. Meaning, that for the final implementation *influence* cannot be chosen too small. Thus ensuring to not mark a change in luminosity as a *signal*. The *influence* parameter does the scaling in the update-function, if an outlier is detected. To achieve this, *lag* was fixed at a value of 50 and *influence* at 0.2, which is reasonable since one wants to minimize memory usage and not use a too small value for *influence*. For the parameters in Table 4.2 an example output can be seen in Figure 4.15. After a parameter sweep through different values for *threshold*, ranging from 2 to 5 in 0.1 steps, a value of 3.5 was chosen. This value yielded the best results.

lag	50
influence	0.2
threshold	3.5

Table 4.2: Example parameters

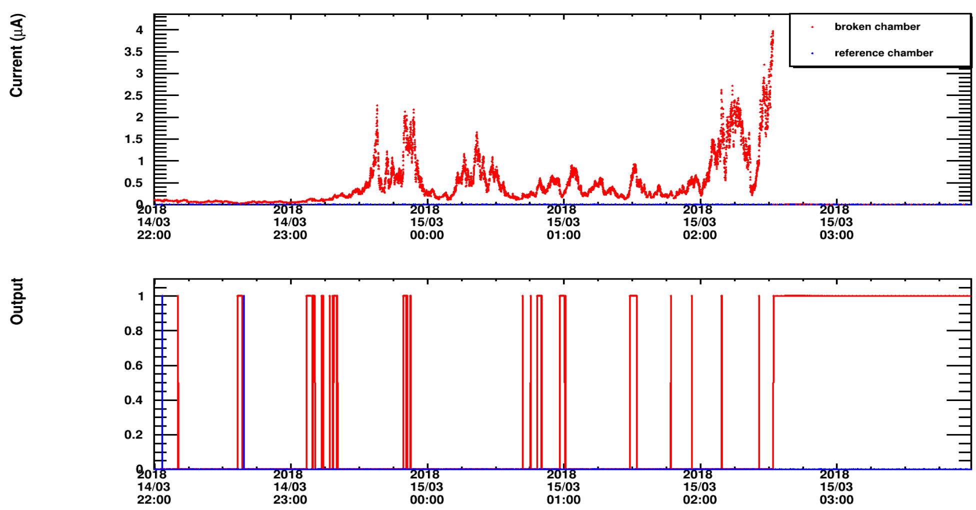

Figure 4.15: This figure shows the measured anode currents of a working chamber and a chamber, exhibiting a chaotic current. The reference chamber output is that of a constant current. Data was taken at low luminosity, which is why the current of the failing chamber is so surprising. The lower figure shows the output of the chaotic current detection algorithm: 1 representing a detected *signal* and 0 an accepted behaviour.

One can already tell from looking at Figure 4.15 that the produced output seems to be very promising. The output at low luminosity of the defect chamber is so surprising since other chambers show a constant output near zero. The algorithm provides a binary output: 1 representing a detected *signal* and 0 an accepted behaviour. Although further analysis into the methodology and parameters is required to determine, which parameters yield the best output. Instead of manually checking all 522 chambers and looking for strange currents, one could imagine a panel of all chambers and the algorithm marks all chambers, exhibiting these chaotic currents. The algorithm could thus at least take care of the need to monitor all 522 chambers. One could then just manually check the chambers producing a lot of *signal*. Making monitoring the ALICE TRD chambers for this type of chaotic current easier.

A large not originally planned repair campaign was already conducted during the currently ongoing long shutdown. The repair campaign was concluded in December 2019. Half of the 18 supermodules were extracted and non-invasively repaired by milling a small hole into the supermodule and removing the capacitors in the resistor chain. While not being able to remove these capacitors in all supermodules due to time constraints, this again allowed for maximum possible efficiency. Five chambers were built without these capacitors in the first place. If chambers without these capacitors produce similar chaotic currents, the problem has a different origin and thus imminent detection of strange currents is very important.

4.4 Van der Meer scans

During van der Meer scans, see Section 2.5.2, a clear correlation between V0 trigger rate and anode current is visible, see Figure 4.16. This hints at the possibility of using these scans with the TRD. In the following this is explored.

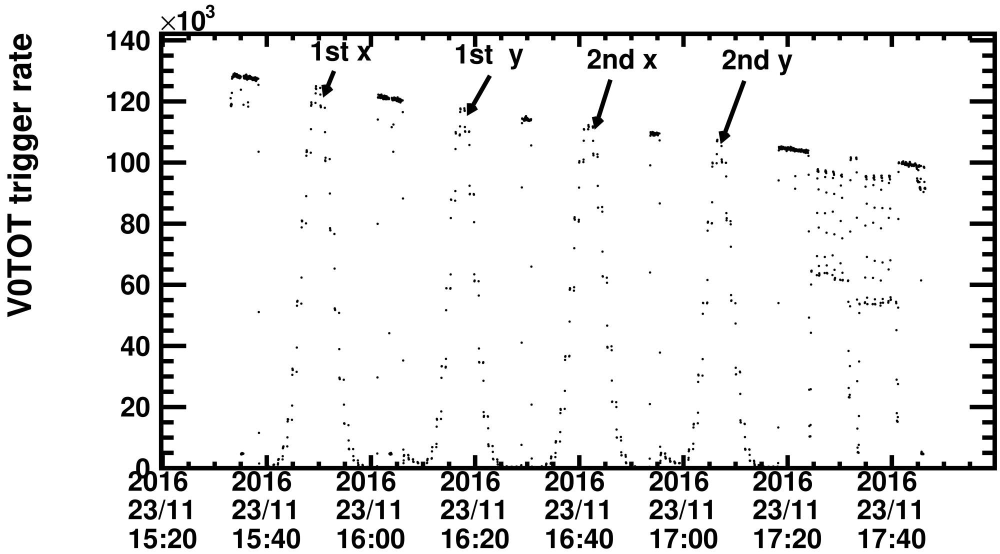

(a) van der Meer scan of the V0 rate, one can see the exponential decay and 4 Gaussians, 2 in x-direction, 2 in y-direction, respectively.

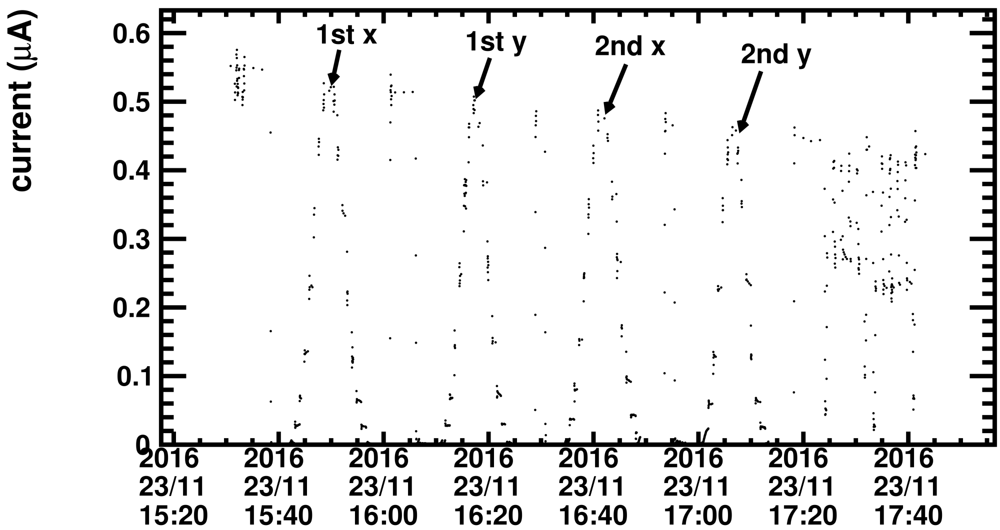

(b) Same scan as above, now with anode currents from the TRD, producing a similar output.

Figure 4.16: vdM scan Fill 5553 in pp collision at $\sqrt{s} = 13$ TeV.

As already explained, the bunch intensities will decay over time. To correct this, plateaus are measured in the form of head-on collisions in between the scans. The exponential decay of the bunch intensities can then be corrected by fitting an exponential model to these plateau regions. This correction had little impact on the result. The first two Gaussians were chosen for analysis, one in x-direction and one in y-direction.

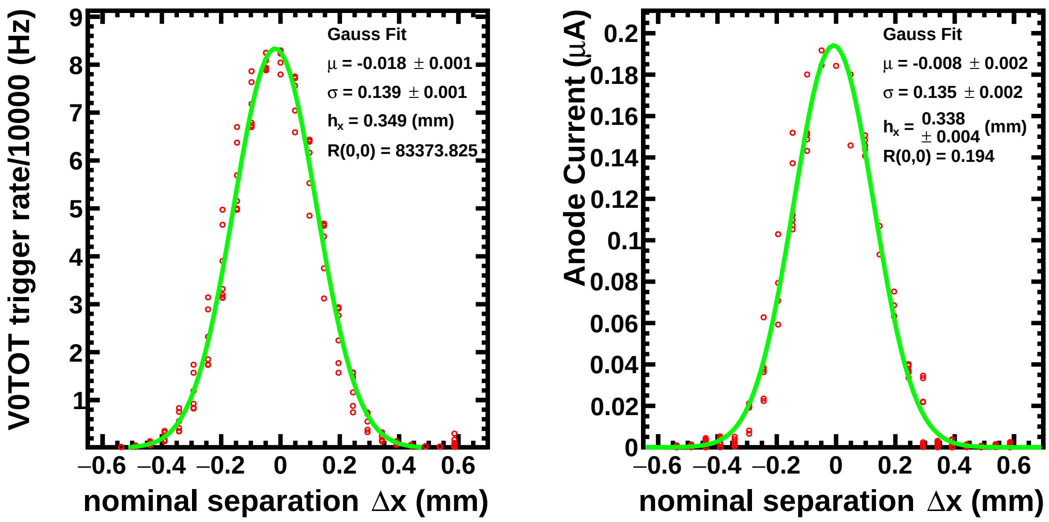

(a) Effective beam width in x-direction, h_x.

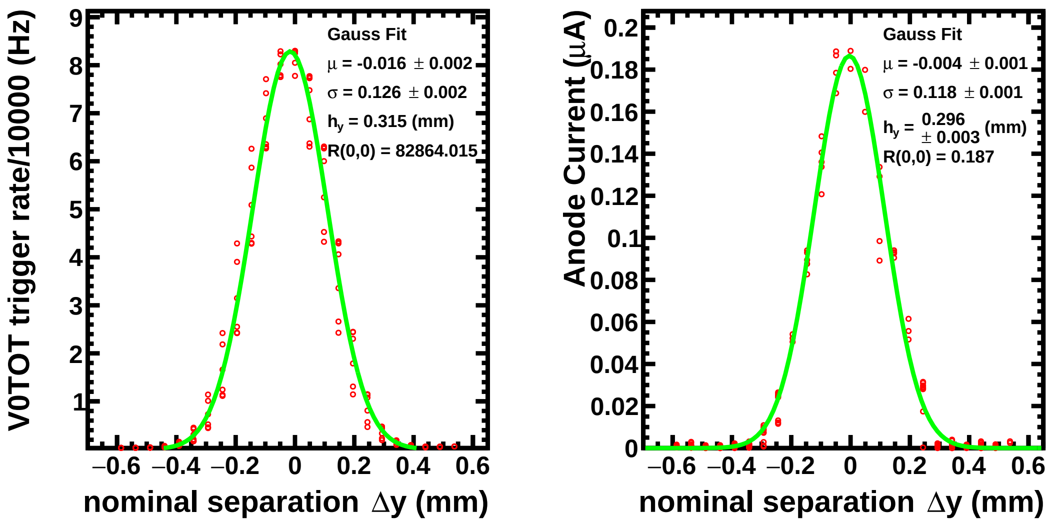

(b) Effective beam width in y-direction, h_y.

Figure 4.17: Measurements of the effective beam widths using the assumptions above.

Results for one chamber are presented in Figure 4.17. As expected, the V0 rate and the TRD current follow a Gaussian distribution. The results, captured in Table 4.3, deviate significantly from each other.

	V0 rate	anode current
h_x (mm)	0.349±0.000	0.338±0.004
h_y (mm)	0.315±0.000	0.296±0.003
$\sigma_{visible}$ (μm)	0.10994	0.10005±0.00016

Table 4.3: Results of the vdM scan.

The non concurrent data sets had to be aligned as described in Section 3.5, which is the biggest source for uncertainties. Additionally, no uncertainties were used for either the V0 and TRD data as they were not available. Furthermore, the TRD is further away from the collision point than the V0 detector. This leads to a smaller visible cross section for the TRD, as particles are absorbed, knocked out in the material in front of the detector or do not even reach the detector any more.

The uncertainties of $h_{x/y}$ for the V0 rates seemingly disappear due to division by the much larger head-on collision rate. Here, a more rigorous treatment for the uncertainties is necessary. Additionally, as already pointed out, only the exponential decay was corrected for. Effects like pile-up affect detectors like the V0, which are closer to the interaction point, more, than the single chambers of the TRD, located at a much larger radius.

Nonetheless, it was concluded that the results are close enough to warrant further analysis. As stated in the beginning of Chapter 4, the goal was to examine the possibility of another independent luminosity determination. The ALICE TRD is clearly able to provide this crucial information.

5 | Summary and Outlook

In this thesis, the anode currents of the ALICE Transition Radiation Detector at high luminosities were analysed. The goal was to develop a better understanding of these currents for Run 3. A better understanding is crucial as in Run 3 the detector will be operated at higher interaction rates than in the previous Runs. The results of this thesis facilitate the usage of the TRD as luminosity meter for ALICE in Run 3. For this one has to know, if the anode currents are stable at these luminosities and their correlation. Furthermore, a way to monitor the anode currents for chaotic currents was implemented to provide high voltage quality assurance.

In the first part, the correlation of the luminosity and anode currents was parametrised. This is done by a linear fit. Tests performed in Run 2 in pp collision at $\sqrt{s} = 13$ TeV, at the same expected luminosities as in Run 3, were analysed. As the tests performed in 2017 only contained averaged luminosity measurements, they were less granular than the ones performed in 2018. However, the tests in 2017 already gave a first glimpse into an expected linear correlation of the luminosity and anode currents. Here, for example, the anode current from channel 06_0_1 was fitted with the function $f(x) = (0.027 \pm 0.006)\,(\mu A) + (0.071 \pm 0.001)\left(\frac{\mu A}{Hz/\mu b}\right) \cdot x$, where x is the luminosity in $(Hz/\mu b)$. Afterwards, the applied weights were discussed. As expected, the anode currents are correlated to the chamber size and the full solid angle coverage. In order to eliminate these effects, one weighted the anode currents with these features. Furthermore, a dependency on both layer and stack position for the produced anode current was found. Next, the distribution of all fit parameters was investigated, specifically the slope parameter. The offset did not follow any discernable distribution as this "defect" (LHC luminosity equals zero, no current should be measurable) of a channel or the power supply was corrected for by subtracting the current measured during cosmic muon runs. The width of distribution of the slope parameter is mainly due to a positional dependency of a chamber. For example, stack 0 is close to the metal door of the magnet, where additional particle scattering induces a higher overall current. Stack 4, although geometrically the same as stack 0, is close the muon absorber where particles are absorbed, reducing the current. Stack $1-3$ behave similar with the weight for the covered solid angle.

Other fills from 2018 contained more granular information about the luminosity, as they were provided by the EMCal detector. The fills confirmed undoubtedly the linear correlation, even up to 120 $Hz/\mu b$. Then the distributions of the fit parameters stemming from the three separate measurements were compared. They were encouragingly similar, the only small deviation was attributed to a pressure change during the day of measurement mitigated by a change in the N_2 gas content. Both are easily correctable for future measurements. This shows that the anode currents are operating stable and produce reproducible measurements at these high luminosities.

The second part of the thesis deals with an algorithm for the detection of chaotic currents. This is especially needed since one can prolong the lifetime of a chamber by identifying these chambers early and reducing the applied voltage. It was shown that the simple yet powerful algorithm could be a way to monitor all chambers for this type of current more effectively. This provides the needed high voltage quality assurance. However, the chosen parameters need further optimisation and the effectiveness of the algorithm in detecting these currents should be compared to other algorithms.

The third and last part shows that one can calculate a visible cross section from van der Meer scans with the anode currents. The calculated visible cross sections from the V0 rate and the TRD currents deviate significantly (62σ). This was attributed to the facts, that pile-up events affect the V0 detector more than a single chamber of the TRD and that the V0 detector sees a larger visible cross section due to its nearness to the interaction point compared to the TRD. Nonetheless, the results look very promising. Combining this with the results from the first part provides directly the necessary tools for the development of a luminosity meter.

The biggest challenge within the work for this thesis was aligning the data sets of the different detectors due to non concurrent data taking between them. This also represents the biggest source of uncertainty in the analyses. Especially, in the case of the van der Meer scans the few data points for each nominal step size lead to misalignment. This effect can be reduced, if the interval one compares the V0 detector luminosity with the anode currents, is chosen smaller. However, this in turn leads to even fewer available data points, reducing the precision of the Gaussian fits. Finding the right balance was quite tricky. Generally for all studies of the thesis, it would be better to have future data sets incorporating the measured quantities simultaneously.

The analyses performed in this thesis showed that the anode currents of the TRD offer a wide range of applicability, ranging from the required tools for the implementation of a luminosity meter, the detection of chaotic currents to calculating visible cross sections from van der Meer scans with the TRD. Especially, it is now possible to develop a luminosity meter with the provided analyses. Further, with the luminosity provided by the TRD one will be able to correct more accurately the space-charge distortions in the ALICE Time Projection Chamber in LHC Run 3. Stable operation at high luminosities and a detailed understanding of the currents as a function of position of TRD currents are crucial for this correction. The results of this thesis positively identify these properties for the high luminosity tests performed in Run 2 and provide the necessary tools to evaluate this for future measurements.

Bibliography

[1] Saranya Samik Ghosh et al. *General Model Independent Searches for Physics Beyond the Standard Model*. Springer International Publishing, 2020. ISBN: 978-3-030-53783-8. DOI: 10.1007/978-3-030-53783-8. URL: https://doi.org/10.1007/978-3-030-53783-8.

[2] P. Braun-Munzinger et al. "Properties of hot and dense matter from relativistic heavy ion collisions". In: *Physics Reports* 621 (Mar. 2016), pp. 76–126. ISSN: 0370-1573. DOI: 10.1016/j.physrep.2015.12.003. URL: http://dx.doi.org/10.1016/j.physrep.2015.12.003.

[3] PDG Collaboration. *J/ψ meson*. Last accessed on 07/01/2021. URL: https://pdglive.lbl.gov/Particle.action?node=M070.

[4] Marten Ole Schmidt. *Space point calibration of the ALICE TPC with track residuals*. Doctoral thesis U. Heidelberg. 2020. DOI: 10.11588/heidok.00028663.

[5] ALICE Collaboration S. Acharya et al. "The ALICE Transition Radiation Detector: construction, operation, and performance". In: *Nucl. Instrum. Meth. A* 881 (2018), pp. 88–127. DOI: 10.1016/j.nima.2017.09.028. arXiv: 1709.02743 [physics.ins-det].

[6] V.L. Ginzburg and I.M. Frank. "Radiation of a uniformly moving electron due to its transition from one medium into another". In: *J. Phys. (USSR)* 9 (1945), pp. 353–362.

[7] John David Jackson. *Classical electrodynamics*. In: American Association of Physics Teachers. 1999.

[8] *ALICE Muon Spectrometer*. Last accessed on 31/01/2021. URL: https://alice-collaboration.web.cern.ch/menu_proj_items/Muon-Spect.

[9] ALICE Collaboration. *ALICE sub-detectors*. Last accessed on 07/01/2021. URL: http://cds.cern.ch/record/2302924.

[10] David Emschermann. "Construction and Performance of the ALICE Transition Radiation Detector". Presented 20 Jan 2010, Doctoral thesis U. Heidelberg. 2010. URL: https://cds.cern.ch/record/1331123.

[11] A. Van Oosterom and J. Strackee. "The Solid Angle of a Plane Triangle". In: *IEEE Transactions on Biomedical Engineering* BME-30.2 (1983), pp. 125–126. DOI: 10.1109/TBME.1983.325207.

[12] Hermann Kolanoski and Norbert Wermes. *Teilchendetektoren.* Springer, 2016.

[13] Luisa Bergmann. "Studies of the Gain and Drift Velocity for the ALICE Transition Radiation Detector at the CERN LHC". Bachelor's Thesis. U. Heidelberg, 2017. URL: https://www.physi.uni-heidelberg.de//Publications/bergmann_bsc_thesis.pdf.

[14] ALICE Collaboration. *ALICE EMCal Physics Performance Report.* 2010. arXiv: 1008.0413.

[15] ALICE Collaboration. "Measurement of visible cross sections in proton-lead collisions at $\sqrt{s_{\mathrm{NN}}} = 5.02$ TeV in van der Meer scans with the ALICE detector". In: *JINST* 9.11 (2014), P11003. DOI: 10.1088/1748-0221/9/11/P11003. arXiv: 1405.1849 [nucl-ex].

[16] Werner Herr and B Muratori. "Concept of luminosity". In: (2006). CAS - CERN Accelerator School: Intermediate Accelerator Physics. DOI: 10.5170/CERN-2006-002.361. URL: https://cds.cern.ch/record/941318.

[17] *Link to facts of the LHC.* Last accessed on 07/01/2021. URL: https://home.cern/resources/faqs/facts-and-figures-about-lhc.

[18] *Link to Author's GitHub.* URL: https://github.com/dogg0w0/ALICE_TRD_hv_analysis.

[19] *Minjung Kim.* Last accessed on 07/01/2021. URL: https://www.physi.uni-heidelberg.de/Mitarbeiter/madetails.php?id=492.

[20] *Links to the data sets.* Last accessed on 07/01/2021. URL: https://cernbox.cern.ch/index.php/s/GrlbrUz6jAp8Inx.

[21] *Link to ALICE logbook.* Last accessed on 07/01/2021. URL: https://alice-logbook.cern.ch/logbook/date_online.php?p_cont=comd&p_cid=574436.

[22] J.P.G van Brakel. *Robust peak detection algorithm using z-scores.* Last accessed on 07/01/2021. 2014. URL: https://stackoverflow.com/questions/22583391/peak-signal-detection-in-realtime-timeseries-data/22640362#22640362.

[23] *Link to vdM input files.* Last accessed on 07/01/2021. URL: https://home.saske.sk/~kralik/VdM/VdM-allin1file/.

[24] ALICE Collaboration. "Radiation Dose and Fluence in ALICE after LS2". In: (Oct. 2018). ALICE-PUBLIC-2018-012. URL: https://cds.cern.ch/record/2642401.

Appendix

- The operation status of the ALICE TRD channels in 2017 is displayed in Figure 5.1.
- The operation status of the ALICE TRD channels in 2018 is displayed in Figure 5.2.
- A complete example of the linear fit of luminosity vs anode current in sector 6 in Fill 6168 and Fill 6169 pp collision at $\sqrt{s} = 13$ TeV is given in Figure 5.3.
- Similar graphics presented in Section 4.1 with the chamber sizes and gains as weights are shown in Figure 5.4, little difference is observe in comparison.
- An example fit for a single chamber in Fill 7122, Fill 7133 and Fill 7135 pp collisions at $\sqrt{s} = 13$ TeV in 2018 is presented in Figure 5.5.
- The distributions of slope parameters with the chamber sizes as a weight in Fill 7122, Fill 7133 and Fill 7135 pp collisions at $\sqrt{s} = 13$ TeV in 2018 is presented in Figure 5.6.
- The gas mixture composition in Fill 7133 and Fill 7135 pp collisions at $\sqrt{s} = 13$ TeV in 2018 is presented in Figure 5.7.

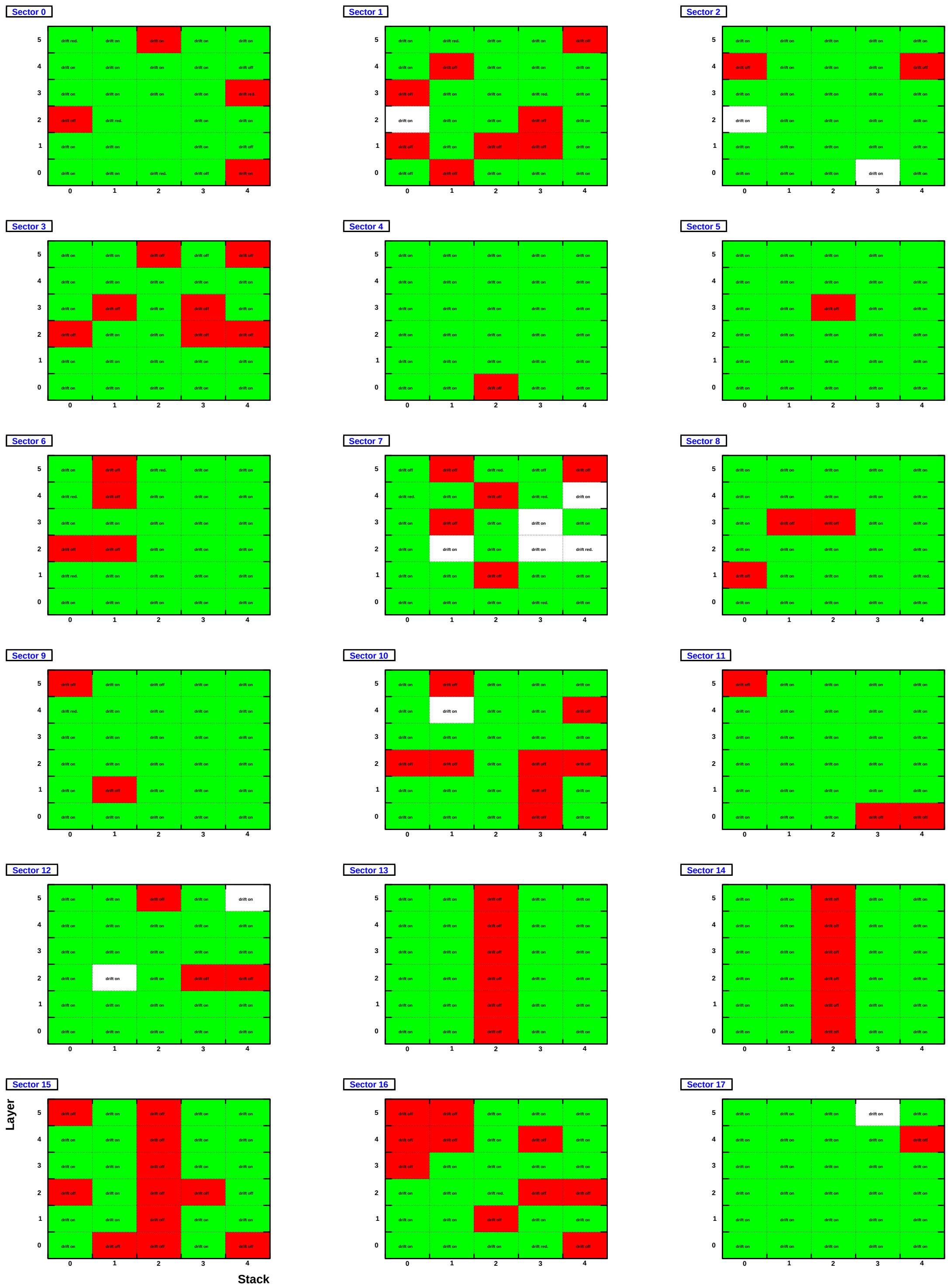

Figure 5.1: Operation status of ALICE TRD channels in 2017

Anode current: Green=ok, White=reduced, Red=off

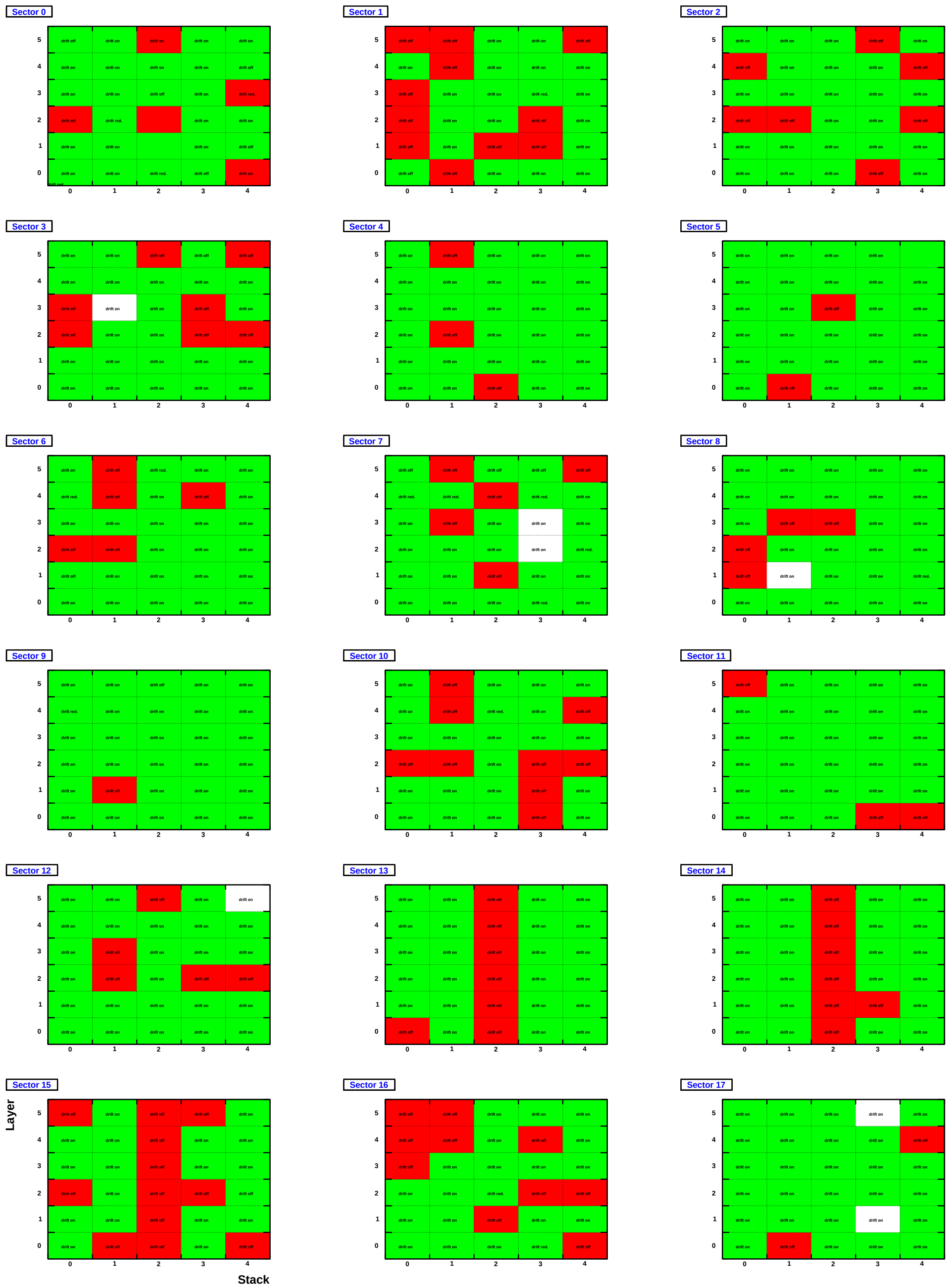

Figure 5.2: Operation status of ALICE TRD channels 2018

Anode current: Green=ok, White=reduced, Red=off

Fit Parameters 2017

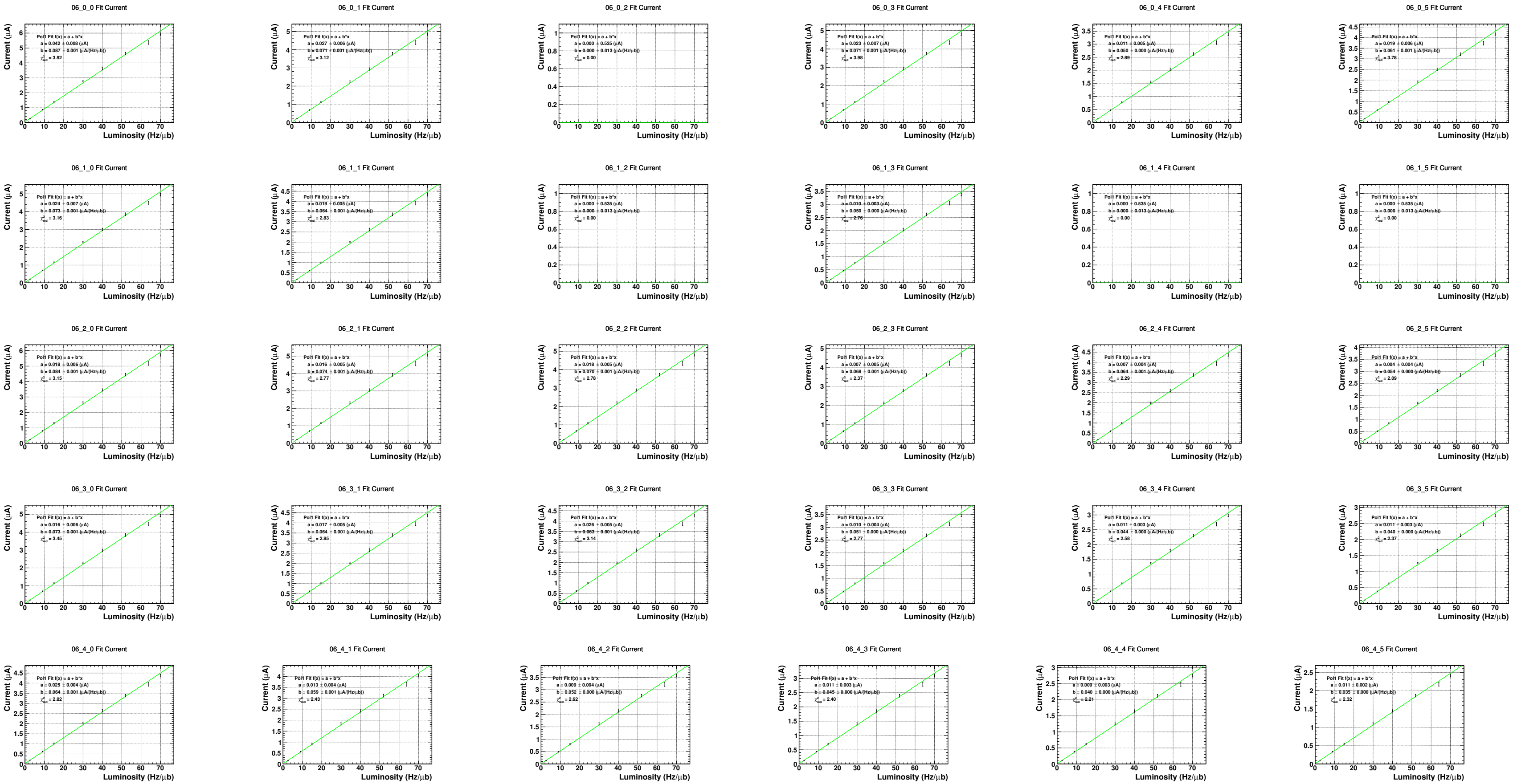

Figure 5.3: Linear Fits for sector 6.

Gain Weight

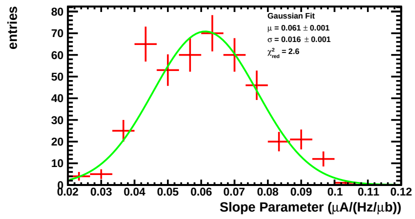

(a) Slope parameter distribution.

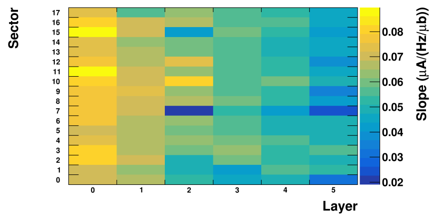

(b) Slope parameter of all layers.

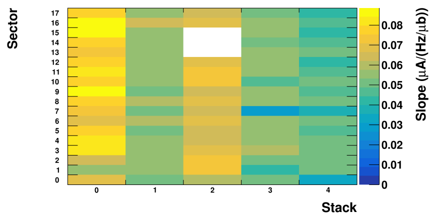

(c) Slope parameter of all stacks.

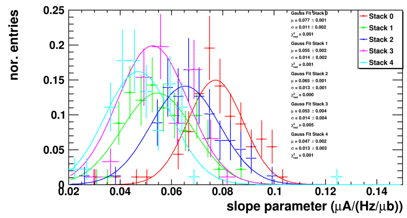

(d) Slope parameter distribution of all stacks.

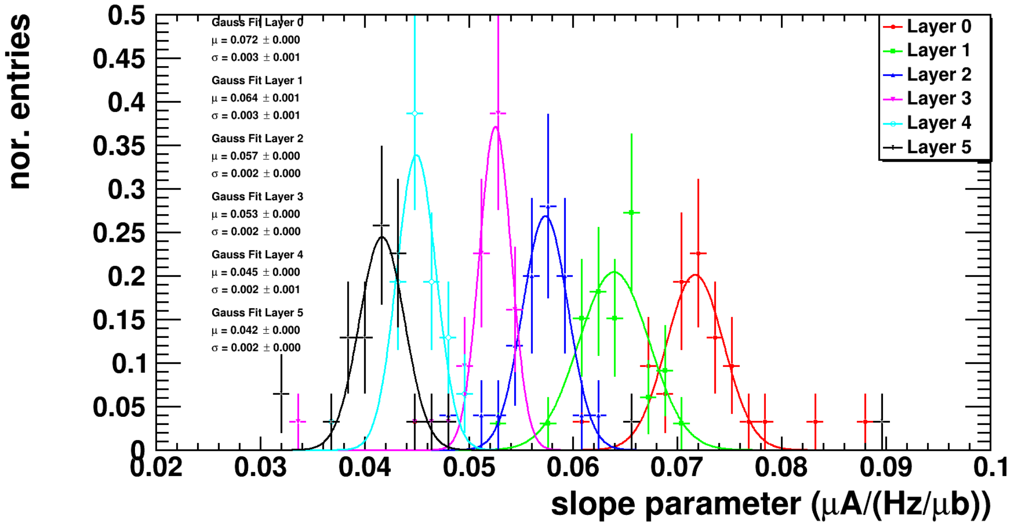

(e) Slope parameter distribution in layers of stack 1 and 3.

Figure 5.4: Plots with gain as an additional weight.

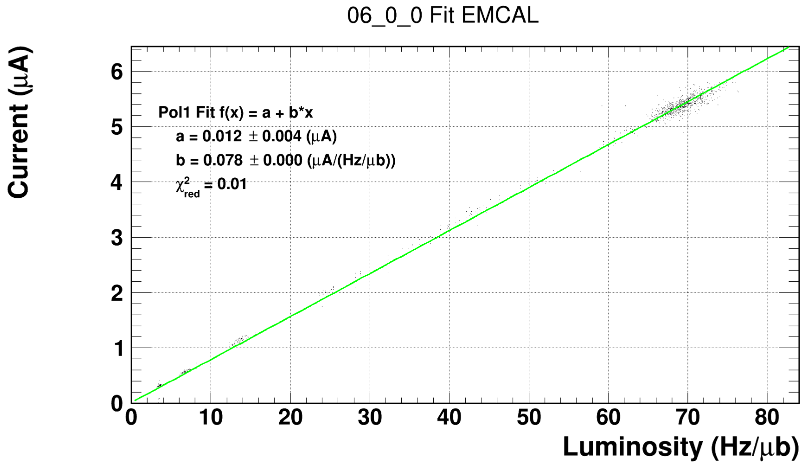

(a) High luminosity measurement in Fill 7122.

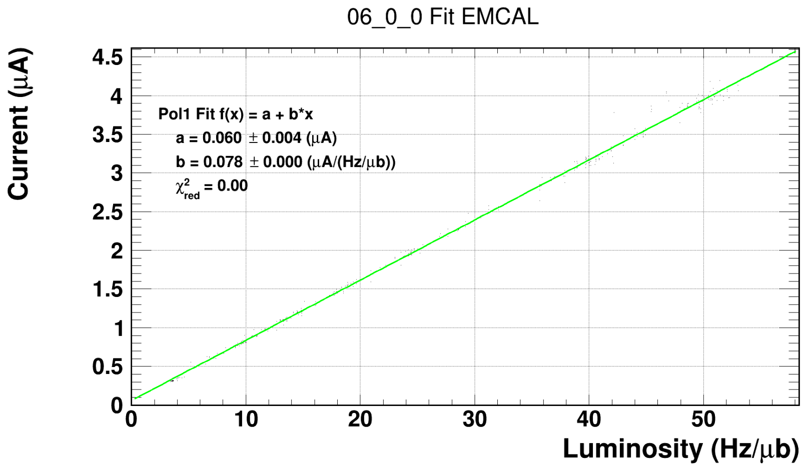

(b) High luminosity measurement in Fill 7133.

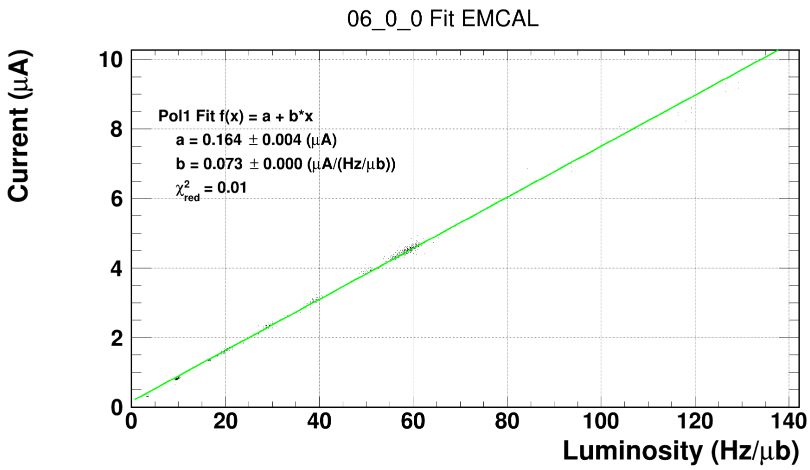

(c) High luminosity measurement in Fill 7135.

Figure 5.5: 2018 luminosity measurements, singular chamber.

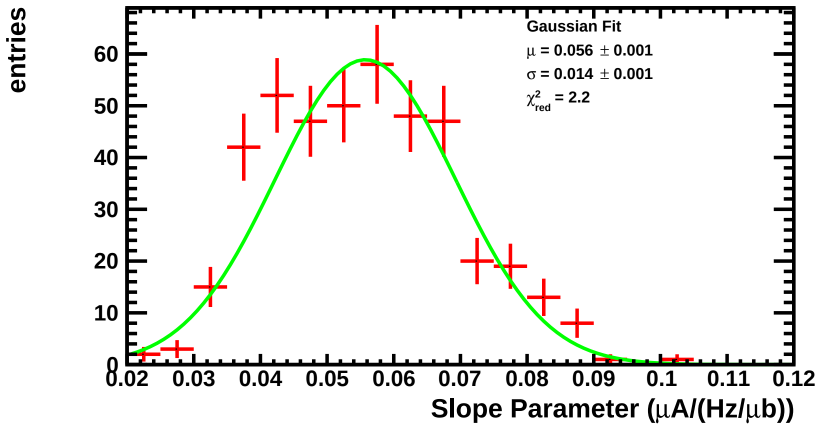

(a) Slope parameter distribution in Fill 7122.

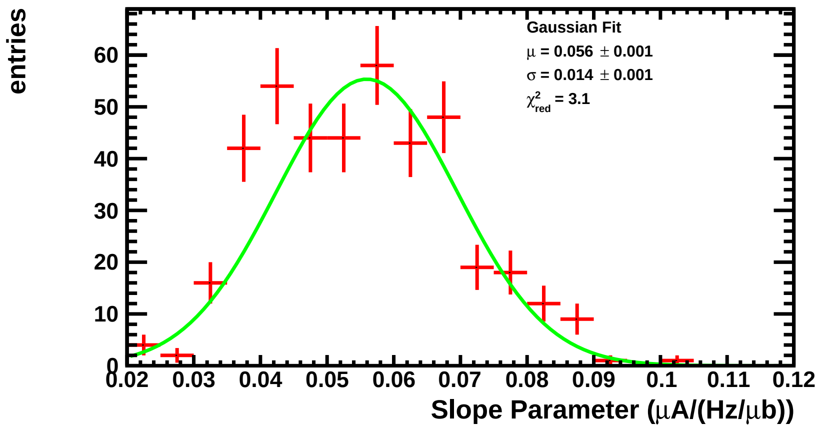

(b) Slope parameter distribution in Fill 7133.

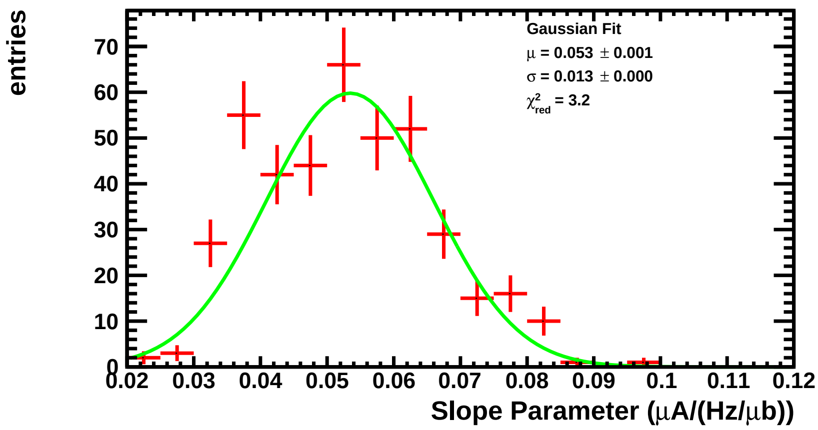

(c) Slope parameter distribution in Fill 7135.

Figure 5.6: 2018 Slope parameter distributions.

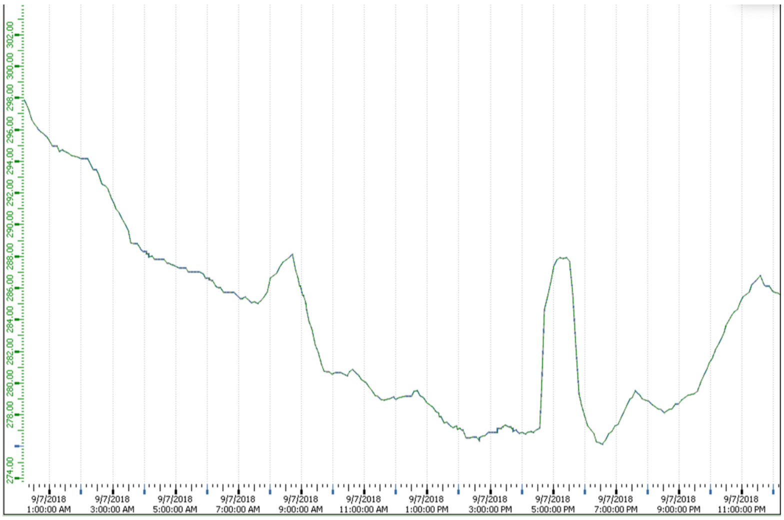

(a) H_2O

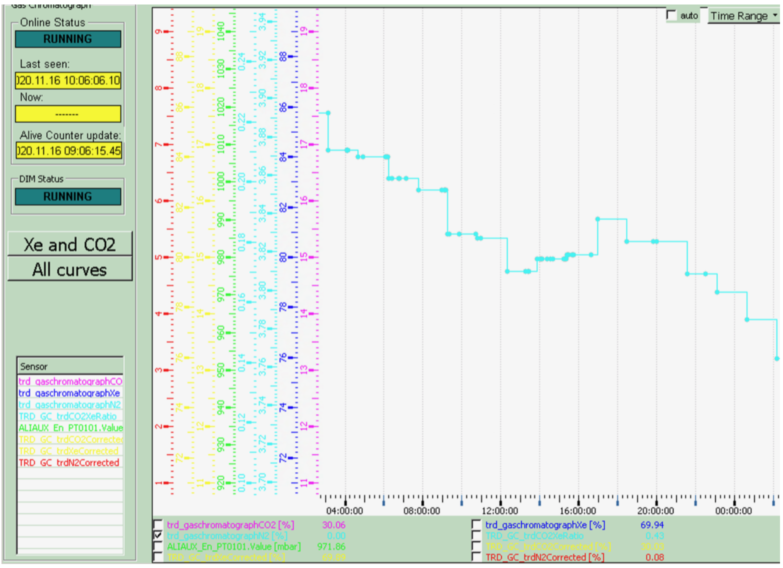

(b) N_2

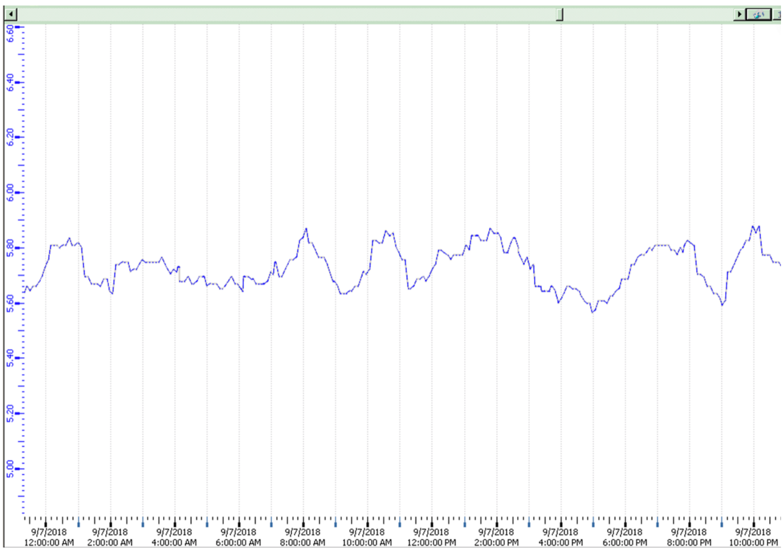

(c) O_2

Figure 5.7: Gas-mixture composition.

Acknowledgements

This was a triumph.
I'm making a note here:
HUGE SUCCESS.

Portal

Still Alive (my favourite video game)

First of all, I would like to thank Priv. Doz. Dr. Yvonne Pachmayer for giving me the opportunity to write my bachelor thesis in the ALICE group. Yvonne Pachmayers continuos support during this interesting endeavour was invaluable. I am truly amazed that even in these strange times her dedication to the scientific process is unwavering. Additionally, I would like to thank Prof. Dr. Klaus Reygers for agreeing to be the second referee for this thesis. I would also like to especially thank Dr. Marten Ole Schmidt for his insightful input and constructive criticism for this thesis. Furthermore, I want to thank my dear friend David Waldmann for proofreading this thesis.

Last but not least, I want to thank the entire ALICE group for all the help I received and providing a joyous work environment.

Again, I am truly humbled and thankful to you all.

Erklärung

Ich versichere, dass ich diese Arbeit selbstständig verfasst und keine anderen als die angegebenen Quellen und Hilfsmittel benutzt habe.

Heidelberg, den 15.02.2021,

Felix Schlepper